AN ABSTRACT OF THE THESIS OF

Manas Behera for the degree of Master of Science in Electrical and Computer Engineering presented on May 18, 2004.
Title: Coupled Circuit and Device Simulations for Design of RF MEMS VCOs.

Abstract approved: _____
Kartikeya Mayaram

A new coupled circuit and electrostatic/mechanical simulator (COSMO) for the design of RF MEMS VCOs is presented in this thesis. The numerical solution of device level equations is used to accurately compute the capacitance of a MEMS capacitor. This coupled with a circuit simulator facilitates the simulation of circuits incorporating MEMS capacitors. Different MEMS capacitor structures are simulated and their effect on VCO performance is studied. In addition, the noise from the MEMS capacitor is combined with a nonlinear circuit-level noise analysis to determine the phase noise of RF MEMS VCO. Simulations of two different MEMS VCO architectures show good agreement with experimentally observed behavior.

Coupled Circuit and Device Simulations for Design of RF MEMS VCOs

by
Manas Behera

A THESIS

submitted to

Oregon State University

in partial fulfillment of
the requirements for the
degree of

Master of Science

Presented May 18, 2004
Commencement June 2005

Master of Science thesis of Manas Behera presented on May 18, 2004.

APPROVED:

Major Professor, representing Electrical and Computer Engineering

---

Director of the School of Electrical Engineering and Computer Science

---

Dean of the Graduate School

I understand that my thesis will become part of the permanent collection of Oregon State University libraries. My signature below authorizes release of my thesis to any reader upon request.

Manas Behera, Author

ACKNOWLEDGEMENTS

I would like to take this opportunity to express my gratitude towards all the people who have made it possible for me to reach this important milestone in life. This thesis would not have been possible without their continuous support, encouragement and inspiration.

I convey my sincere thanks to Dr. Kartikeya Mayaram, my research advisor at OSU, for giving me an opportunity to work on such a novel and promising topic like RF MEMS. Thanks to him I could publish several papers which will always be a big achievement for me. I would like to thank him for his continuous support and ever important guidance during the course of my research. I have always been an admirer of Prof. Mayaram's teaching style. His excellent lectures on analog circuit simulation and RF IC design were highly beneficial for my research. I am also grateful to him for giving me useful tips on writing and presenting technical papers.

This research work would not have attained its present shape without the aid of Prof. Narayan Aluru and his team from the Beckman Institute for Advanced Science and Technology, UIUC. I convey my sincere thanks to Prof. Aluru for providing the device simulator EM8.9. I would also like to offer many thanks to Sudipto De, who is currently doing his Ph.D. under Prof. Aluru, for helping me out with many of the EM8.9 and MEMS related issues. He has always been willing to share his expertise on MEMS and has always been prompt in answering my numerous questions.

In my opinion, the most interesting phase of my research work was working on simulation of phase noise in RF MEMS VCOs. This would not have been possible without the excellent sense of timing of Volodymyr Kratyuk or Vova as we like to call him. I thank Vova for successfully implementing phase noise analysis in SPICE3 and providing me with a platform at the right time.

I am especially thankful to Taras Dudar who was of great help to me during the initial stages of my research work. I would also like to acknowledge Dr. Chenggang Xu and Yutao Hu, who took the trouble to clarify my queries on numerous occasions.

I would like to express my deep appreciation towards Janakiram Sankaranarayan and Maneesha Yellepeddi for their all important comments and feedback on my research work. I wish them all the best with this project and hope they take this work to higher levels.

I am grateful to Dr. Un-Ku Moon, Dr. Gabor Temes and Dr. Terri Fiez for their excellent lectures on Analog IC design. I also thank Dr. Moon, Dr. Chenggang Xu and Prof. David Hackleman for agreeing to serve on my examining committee.

This research has been funded by NSF. I thank them for their support. I would also like to thank Ferne and the entire Electrical and Computer Engineering staff for their help and assistance.

I have a profound sense of gratitude for my late grandparents, my parents and every member of my family for making me a capable human being. I have always looked to them for inspiration. I am especially grateful to my uncle and aunt as well as my brothers and sisters-in-law for their love and support during my stay in the United States. I thank my younger brother, Aasish, for helping me in his own unique way.

I do not have words to describe how thankful I am towards my wife, Prachee. I am grateful to her for being patient and supportive during the toughest times. I have known her for almost ten years now and she has always encouraged me to reach new heights. I thank her for playing a big part in making me who I am today.

Finally, I thank all my friends and colleagues here at OSU for their moral support and making my stay here enjoyable.

TABLE OF CONTENTS

Page

1 INTRODUCTION..... 1

1.1 Motivation 1

1.2 Thesis Organization 3

2 THEORETICAL BACKGROUND 5

2.1 Coupled Circuit and Device Simulation..... 5

2.2 Circuit Simulators 7

2.3 Capacitor Stamping……. 9

2.3.1 Stamping a Linear Capacitor…….9
2.3.2 Stamping a Nonlinear Capacitor ……....12

2.4 Device Simulators……..15

2.4.1 Underlying Principle……...15
2.4.2 Methods for Electromechanical Analysis……...16

3 MEMS-BASED CAPACITORS…….....19

3.1 Introduction……19

3.2 Working Principle……..20

3.3 MEMS Variable Capacitor Structures……23

3.3.1 Cantilever Beam and Fixed-Fixed Beam Capacitor…….24
3.3.2 Two-Parallel-Plate MEMS Capacitor with Suspension Structure……...25
3.3.3 Wide Tuning Range Three-Parallel-Plate MEMS Capacitor……..28

TABLE OF CONTENTS (Continued)

Page

3.4 Lumped Equivalent Models for MEMS Capacitors……...30

3.5 Dynamic Characteristics…….....33

4 COSMO: COUPLED SIMULATOR FOR MEMS OSCILLATOR……37

4.1 Introduction……37

4.2 Device Simulations and Capacitance Computation……...39

4.3 Coupling Description for Static Simulations…….43

4.4 Coupling Description for Dynamic Simulations……45

4.5 MEMS VCO Circuit for Simulation of Tuning Characteristics…….48

4.6 Static Simulation Results and Validation with Experimental Data 49

4.6.1 Simulated Tuning Characteristics of Cantilever Beam and Fixed-Fixed Beam Capacitors……..50
4.6.2 Simulated Tuning Characteristics of the Two-Parallel-Plate Capacitor……...……52
4.6.3 Simulated Tuning Characteristics of the Three-Parallel-Plate Capacitor……...……56
4.6.4 Summary and Comparisons……..……58

4.7 Dynamic Simulation Results……..60

4.8 Summary and Missing Effects in COSMO……63
4.8.1 Residual Stress……..64
4.8.2 Effect of Holes in the Top Plate of MEMS Capacitors……..65

5 SIMULATION OF PHASE NOISE IN RF MEMS VCOs…….66

5.1 Introduction……...66

TABLE OF CONTENTS (Continued)

Page

5.2 Phase Noise in RF MEMS VCOs……..67

5.2.1 Phase Noise from Electrical Noise Sources…….68
5.2.2 Brownian-Motion-Induced Phase Noise……..70

5.3 Phase Noise Simulations……75

5.4 MEMS VCO Design for Phase Noise Simulations……78

5.4.1 The VCO Circuit……...78
5.4.2 MEMS Variable Capacitor Design…….....81

5.5 Simulation Results and Validation with Experimental Data……..81

5.6 Summary……...…….87

6 CONCLUSIONS..... 88

6.1 Summary……...88

6.2 Future Work……...……...88

BIBLIOGRAPHY .....…90

APPENDICES ……....92

APPENDIX A MEMS Capacitor Model Parameters …..……...93

APPENDIX B Input Syntax for the MEMS Capacitor Device……...95

LIST OF FIGURES

Figure Page

2.1 Block diagram for interfacing a numerical device simulator into a circuit simulator. …..…….....6

2.2 Linear capacitor. …….……10

2.3 Companion model for stamping a linear capacitor. ……..….12

2.4 Nonlinear capacitor represented as a nonlinear resistor and a current source after time discretization at the n^{th} timepoint. ……..….13

2.5 Companion model for stamping a nonlinear capacitor. …….....14

3.1 Functional model of an electro-mechanically tunable parallel-plate capacitor. ……..21

3.2 Cantilever beam and fixed-fixed beam capacitor. ……..24

3.3 Top view and cross-sectional view of the two-parallel-plate capacitor. ……27

3.4 Wide tuning range three-parallel-plate capacitor. ……..……28

3.5 Modeling the MEMS capacitor in the coupled simulation environment. …..30

3.6 Lumped element model for the two-parallel-plate MEMS capacitor. ……...31

3.7 Series-to-parallel transformation. ……...32

3.8 Lumped element model for the three-parallel-plate MEMS capacitor. ….....33

3.9 Mass-spring-damper model of the MEMS capacitor. ……....34

3.10 Linear system representation of the MEMS variable capacitor. ……....35

3.11 Frequency response of the input force to displacement transfer function. …..36

LIST OF FIGURES (Continued)

Figure Page

4.1 Capacitance computation of the MEMS capacitor. ……..…….40

4.2 Computed capacitance as a function of voltage for a MEMS capacitor…….42

4.3 The COSMO simulator showing coupling between SPICE3 and EM8.9. …44

4.4 The time stepping scheme used in COSMO for dynamic simulations. …….47

4.5 VCO circuit for simulation of tuning characteristics. ……....48

4.6 Capacitance as a function of voltage for cantilever beam capacitors and fixed-fixed beam capacitors. ……..51

4.7 Frequency as a function of voltage for cantilever beam capacitors and fixed-fixed beam capacitors. ……..51

4.8 Capacitance as a function of voltage for different thicknesses of the top plate.…….....53

4.9 Capacitance as a function of voltage for the two-parallel-plate capacitor. 55

4.10 Frequency as a function of voltage for the two-parallel-plate capacitor. …...55

4.11 Capacitance as a function of voltage for the three-parallel-plate capacitor. ..57

4.12 Frequency as a function of voltage for the three-parallel-plate capacitor. …57

4.13 Step response of a fixed-fixed beam capacitor. ……..61

4.14 Comparison of step response of MEMS capacitor obtained from EM8.9 and COSMO. ……...……...62

5.1 MEMS-based parallel LC-tuned oscillator. ……..….67

LIST OF FIGURES (Continued)

Figure Page

5.2 Displacement noise power spectral density. ……..71

5.3 Theoretical phase noise profiles of a MEMS VCO. ……..74

5.4 VCO circuit for phase noise simulations. ……...……...80

5.5 Capacitance as a function of voltage for the MEMS capacitor. …….……...82

5.6 Simulated phase noise spectrum (Q_M=1) of the MEMS VCO and contribution of the different noise sources. ……..……..…….84

5.7 Simulated phase noise spectrum (Q_M = 1, 5, 15) of MEMS VCO. ……...…85

LIST OF TABLES

Table Page

4.1 Design parameters and parasitics for different materials. ……..53

4.2 Comparison of different MEMS capacitor structures. ……...59

4.3 Comparison of simulated results with theoretical calculations and experimental data. ……..59

5.1 Comparison between simulation and measurement results based on the same initial design (ω_n = 30 kHz, ω_o = 800 MHz). …….83

5.2 Summary of phase noise simulations and comparison with measured data...86

To my late grandparents

COUPLED CIRCUIT AND DEVICE SIMULATIONS FOR DESIGN OF RF MEMS VCOS

1 INTRODUCTION

1.1 Motivation

The concept of a coupled circuit and device simulator has proved to be extremely beneficial in the domain of integrated circuits. Since the development of MEDUSA [1], in the early 1980s, significant work has been done in the field of coupled simulation. In the late 1980's, research work was focused on a mixed-level circuit simulator CODECS [2] which can be used to simulate circuits containing diodes, MOSFETS and BJTs that were described using two-dimensional numerical models. In the early 1990's, three-dimensional (3D) device simulators were coupled to the circuit simulator SPICE3 [3] to study the single-event upset (SEU) phenomenon in static random access memory (SRAM) cells [4]. Since the computational costs of these simulators are high, they are not used on a routine basis. However, there are several critical applications in which these simulators are extremely valuable. These include simulation of RF circuits, SEU simulation of

memories, simulation of power devices, and validation of nonquasistatic MOSFET models [5].

Recent research work shows that coupled circuit and device simulations are extremely important for the study of micro-electro-mechanical systems (MEMS) [6], [7]. A coupled simulator can facilitate accurate simulations of these systems even in the absence of proper macromodels for the MEMS devices. Different devices can be simulated using physics-based numerical models when there are stringent accuracy requirements on the simulated results. The behavior of different device structures can also be analyzed without having to construct a macromodel for each structure.

Recently, different configurations of the MEMS-based capacitor have been examined for improved tuning range. In addition to having a high Q factor and a wide tuning range, MEMS variable capacitors can also withstand large voltage swings, thus making them suitable for low phase noise voltage-controlled oscillator (VCO) applications. However, the absence of an accurate model for the MEMS variable capacitor has made it difficult to simulate the behavior of MEMS VCOs. This results in an extremely long design cycle or conservative design practices.

As a possible solution to these problems, this research focuses on the development of a coupled circuit and device simulator, COSMO, for the improved design of MEMS-capacitor based RF VCOs. COSMO uses coupled simulations to efficiently simulate the tuning characteristics and phase noise in RF MEMS VCOs.

Comparisons between simulated results and existing experimental data are used to demonstrate the accuracy of this approach.

1.2 Thesis Organization

This thesis is organized into six chapters. In Chapter 1, an introduction to coupled circuit and device simulation is presented and the motivation behind this work is discussed.

Chapter 2 addresses the theoretical background. A general coupled circuit and device simulation environment is described and an overview of circuit and device simulators is presented. A detailed description of stamping a linear and a nonlinear capacitor in the circuit matrix is also presented. In addition, the underlying principle of device simulations and methods for electromechanical analysis are discussed.

In Chapter 3, the working principle of MEMS variable capacitors is described. Device characteristics and design considerations are illustrated. An overview of the different configurations of the MEMS variable capacitors employed in this work is presented. Furthermore, lumped equivalent models for the MEMS variable capacitors, necessary for their accurate simulation are presented.

Chapter 4 describes the development of the coupled circuit and device simulator in detail. A method for the accurate computation of the capacitance of a MEMS capacitor is presented. Coupling algorithms for accurate static and dynamic simulations are described. The effects of different MEMS capacitor structures and materials on the tuning characteristics of a VCO are illustrated and comparisons with experimentally observed behavior are presented. The simulated dynamic behavior of MEMS variable capacitors is presented and its effect on the simulation of RF VCOs is discussed.

In Chapter 5, a detailed analysis of phase noise in RF MEMS VCOs is provided. An overview of the simulation environment employed for the accurate simulation of phase noise is presented. The simulated phase noise characteristics are compared with theoretical deductions and experimental data. In addition, important issues in the phase noise characteristics of RF MEMS VCOs are addressed.

The final chapter, Chapter 6, summarizes important results of this research and concludes with suggestions for future work.

2 Theoretical Background

2.1 Coupled Circuit and Device Simulation

Coupled circuit and device simulators consist of circuit simulators integrated with numerical device solvers. These simulators facilitate accurate simulations of advanced devices and physical effects not available in standard circuit simulations. In addition, during the device design phases of development, coupled simulations can be used for design verification without the need for extracting new models or model parameters. Different non-electronic components can be simulated by these simulators. Hence, coupled circuit and device simulations are extremely important for the study of mixed-technology systems where different types of on-chip components for sensing, actuation, data storage, and information processing are integrated together.

A device-level simulator provides the solution of device characteristics based on partial differential equations describing the physical operation of the device. The numerical solution obtained from the device simulator is used by a circuit simulator to accurately simulate circuits incorporating the device. Fig. 2.1 shows how the two simulators are configured to communicate with each other. Similar to an analytical model such as a BJT or MOSFET, a numerical device represents another block in the circuit simulator. This block communicates with the

device simulator through an interface routine which uses an efficient coupling algorithm to accurately solve circuits incorporating numerical devices. Development of efficient coupling algorithms and prudent interface designs constitute the main challenge in the creation of coupled circuit and device simulators.

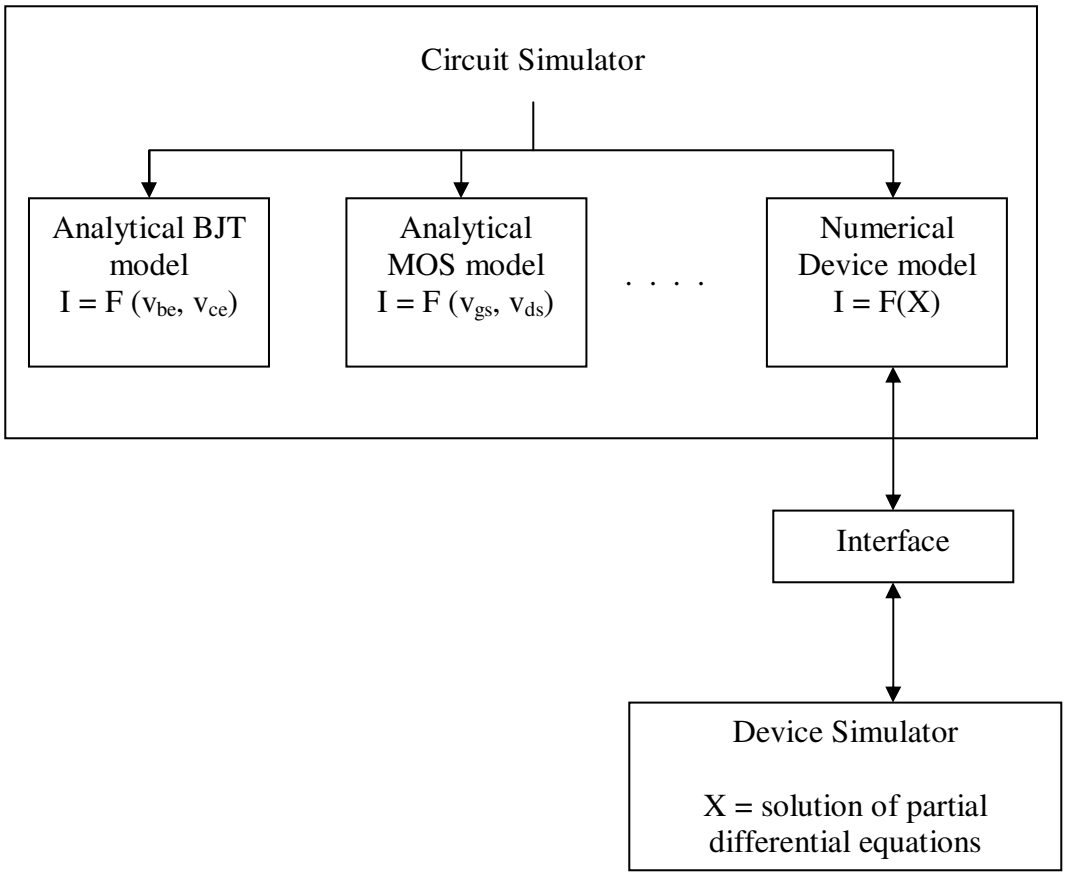

Fig. 2.1. Block diagram for interfacing a numerical device simulator into a circuit simulator.

2.2 Circuit Simulators

A typical circuit simulator like SPICE3 solves non-linear circuit equations by a modified form of the Newton-Raphson (NR) method [8]. The non-linear system of equations for the circuit can be represented as

$$F(V) = 0 \tag{2.1}$$

where V is the vector of node voltages in the circuit, and F represents the sum of the currents flowing into each node in the circuit and both V and F have dimensions equal to the number of nodes in the circuit N. Equation (2.1) is a direct consequence of Kirchoff's current law.

Applying the Newton-Raphson (NR) method to (2.1) yields a linear system of equations which can be expressed as

$$V^{(i+1)} = V^i - J^{-1}(V^i)F(V^i) \tag{2.2}$$

where $J(V^i)$ is the Jacobian at the i^{th} Newton iteration and is given as (2.3).

$$J(V)=\begin{bmatrix} \frac{\partial F_1}{\partial V_1} & \frac{\partial F_1}{\partial V_2} & \cdots & \frac{\partial F_1}{\partial V_N} \\ \frac{\partial F_2}{\partial V_1} & \frac{\partial F_2}{\partial V_2} & \cdots & \frac{\partial F_2}{\partial V_N} \\ \vdots & & & \\ \frac{\partial F_N}{\partial V_1} & \frac{\partial F_N}{\partial V_2} & \cdots & \frac{\partial F_N}{\partial V_N} \end{bmatrix} \tag{2.3}$$

For each Newton iteration, the previous voltage V^i is known and hence, $V^{(i+1)}$ can be computed. In a circuit interpretation of (2.2) and (2.3), assuming a nodal formulation, each Jacobian element has units of conductance, and therefore, J can be replaced with G as shown in (2.4).

$$G^i V^{(i+1)} = G^i V^i - F^i \tag{2.4}$$

The matrix G^i and vector F^i are evaluated at V^i. The above equation represents a linear circuit since both the coefficient G^i and the RHS of (2.4) are independent of $V^{(i+1)}$. Furthermore, G^i is a linear conductance and $G^i V^i$-F^i can be viewed as a current source. The NR iteration is terminated when convergence is reached meaning that the change in V between two consecutive iterations is smaller than a predefined tolerance.

The most commonly used analysis in the design of VCOs is the time-domain transient analysis. In this analysis, time discretization is performed using an integration method, linearization is done by a Newton-Raphson method, and the algebraic system is solved using sparse matrix techniques. For each time step, the

node voltages are computed, time-integration is applied to capacitors and inductors, and the Jacobian matrix for Newton's method is updated and solved for new values of node voltages. Newton iterations are performed until convergence. In addition, the local truncation error due to the time discretization is checked to determine if the time step is acceptable in terms of accuracy. If this error is too large, the time step is reduced and the computation is repeated.

2.3 Capacitor Stamping

Stamping is the procedure for adding the contribution of a device to a circuit matrix and to the right-hand-side (RHS) vector. In this section, the stamping of a linear capacitor and a nonlinear capacitor is described for transient analysis. The integration method used through out this section is assumed to be of a general form and is given by (2.5).

$$\frac{dX_n}{dt} = \alpha X_n + \beta \tag{2.5}$$

2.3.1 Stamping a Linear Capacitor

In Section 2.2, transient analysis in circuit simulators was described. For each time step, Newton-Raphson iterations are performed until convergence is reached. Consider a linear capacitor with capacitance value *C* as shown in Fig. 2.2.

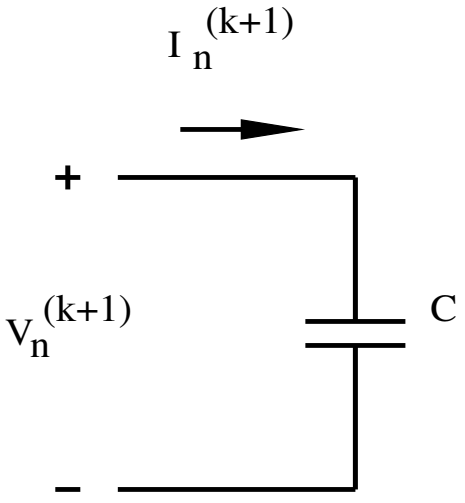

Fig. 2.2 Linear capacitor.

The terminal voltage and current across the capacitor during the $(k+1)^{th}$ iteration of the n^{th} time point are $V_n^{(k+1)}$ and $I_n^{(k+1)}$, respectively. Using (2.5), the current in the capacitor at the n^{th} time point can be expressed in terms of the charge q_n as shown in (2.6).

$$I_n = \frac{dq_n}{dt} = \alpha q_n + \beta \tag{2.6}$$

The current across the capacitor in the $(k+1)^{th}$ iteration is linearized by Newton's method and can be expressed as

$$I_n^{(k+1)} = I_n^{(k)} + \left(V_n^{(k+1)} - V_n^{(k)}\right)\frac{\partial I_n}{\partial V_n}|_k \tag{2.7}$$

Further simplification of (2.7) results in a linear equation given by

$$I_n^{(k+1)} = G_{eq}^{(k)} V_n^{(k+1)} + I_{eq}^{(k)} \tag{2.8}$$

where,

$$G_{eq}^{(k)} = \frac{\partial I_n}{\partial V_n}|_k = \alpha C \tag{2.9}$$

and

$$I_{eq}^{(k)} = I_n^{(k)} - V_n \frac{\partial I_n}{\partial V_n}|_k = I_n^{(k)} - \alpha q_n^{(k)} \tag{2.10}$$

Hence, the linear capacitor can be represented by a linear conductance G_{eq} and a current source I_{eq} which is also known as the companion model as shown in Fig. 2.3.

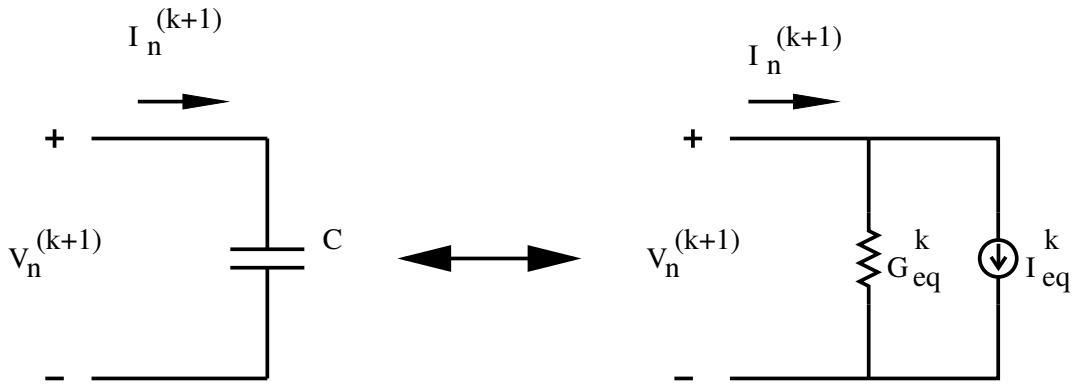

Fig. 2.3 Companion model for stamping a linear capacitor.

Thus, the device contribution to the circuit matrix and to the RHS vector is as shown in (2.11).

$$\begin{array}{c} \\ N+ \\ N- \end{array} \begin{array}{c} \begin{array}{ccccc} \cdots & \cdots & \cdots & \cdots & \cdots \end{array} \\ \begin{bmatrix} \cdots & G_{eq}^{k} & \cdots & -G_{eq}^{k} & \cdots \\ \cdots & \cdots & \cdots & \cdots & \cdots \\ \cdots & -G_{eq}^{k} & \cdots & G_{eq}^{k} & \cdots \end{bmatrix} \end{array} \begin{array}{c} \begin{array}{c} N+ \\ N- \end{array} \\ \begin{bmatrix} V_{+}^{(k+1)} \\ V_{-}^{(k+1)} \end{bmatrix} \end{array} = \begin{array}{c} \text{RHS} \\ \begin{bmatrix} -I_{eq}^{k} \\ I_{eq}^{k} \end{bmatrix} \end{array} \tag{2.11}$$

2.3.2 Stamping a Nonlinear Capacitor

Consider a nonlinear capacitor where the charge, $q = f(v)$, is a nonlinear function of the voltage. From (2.6), the current in the capacitor during the n^{th} time point is given by

$$I_n = \alpha f(V_n) + \beta \tag{2.12}$$

From the above equation it can be seen that the nonlinear capacitor can be represented by a nonlinear resistor ($i = \alpha f(v)$) and a current source (β). Hence, at the n^{th} time point, the companion model for the nonlinear capacitor is as shown in Fig. 2.4.

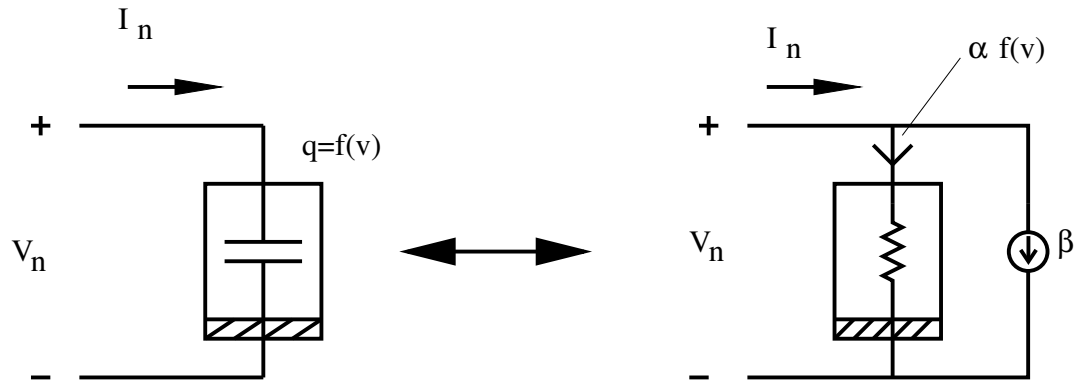

Fig. 2.4 Nonlinear capacitor represented as a nonlinear resistor and a current source after time discretization at the n^{th} timepoint.

Applying Newton's method, the current through the nonlinear resistor is linearized and can be expressed by (2.7). The equivalent conductance and current are given by

$$G_{eq}^{(k)} = \frac{\partial I_n}{\partial V_n}\Big|_k = \alpha f'\left(V_n^{(k)}\right) \tag{2.13}$$

$$I_{eq}^{(k)} = I_n^{(k)} - V_n \frac{\partial I_n}{\partial V_n}|_k = I_n^{(k)} - \alpha V_n^{(k)} f'\left(V_n^{(k)}\right) \tag{2.14}$$

Thus, the nonlinear resistor can be represented by the linear conductance $G_{eq}^{(k)}$ and the current source $I_{eq}^{(k)}$ and the overall companion model of the nonlinear capacitor is as shown in Fig. 2.5.

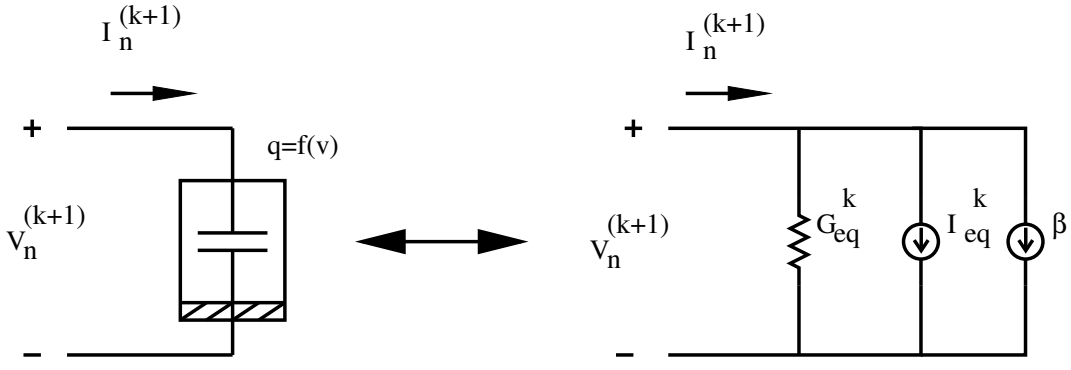

Fig. 2.5 Companion model for stamping a nonlinear capacitor.

Thus, the device contribution to the circuit matrix and to the RHS vector is as shown in (2.15).

$$\begin{array}{c} \\ N+ \\ N- \end{array} \begin{array}{c} \begin{array}{ccccc} & N+ & & N- & \end{array} \\ \begin{bmatrix} \cdots & \cdots & \cdots & \cdots & \cdots \\ \cdots & G_{eq}^k & \cdots & -G_{eq}^k & \cdots \\ \cdots & \cdots & \cdots & \cdots & \cdots \\ \cdots & -G_{eq}^k & \cdots & G_{eq}^k & \cdots \\ \cdots & \cdots & \cdots & \cdots & \cdots \end{bmatrix} \end{array} \begin{bmatrix} \\ V_+^{(k+1)} \\ \\ V_-^{(k+1)} \\ \\ \end{bmatrix} = \begin{array}{c} \text{RHS} \\ \begin{bmatrix} \\ -I_{eq}^k - \beta \\ \\ I_{eq}^k + \beta \\ \\ \end{bmatrix} \end{array} \tag{2.15}$$

2.4 Device Simulators

Device simulation is an important design tool for IC and MEMS technology. It provides an environment for the designer to experiment with different structures by providing insight into the performance of the physical device structure. In addition to being an important aid to the design engineer, research in device simulation has lead to studies and modeling of advanced physical phenomenon for accurate simulations which in turn results in a better understanding of device performance. In this section the underlying principle in device simulators is described and the methods employed specifically for electromechanical analysis are discussed.

2.4.1 Underlying Principle

A device-level simulator provides the solution of device characteristics based on the partial differential equations (PDEs) describing the physical operation of the device. In most cases the PDEs are non-linear in space and time and are obtained from the underlying physics. These equations are solved for applied terminal voltages which constitute the boundary conditions for the PDEs.

The first step towards obtaining the numerical solution of the basic device equations is discretization of the continuous device-simulation problem in both space and time. The simulation domain is divided into smaller regions and the discrete problem is solved for each of these regions with the applied boundary

conditions. Space discretization can be performed by either a finite-difference or a finite-element method in which grids or meshes are generated and discretization is performed by taking these grids into account. Space discretization plays an important role in the overall accuracy of a simulation. As the number of grids is increased, the accuracy of the simulation results improves at the expense of computational efficiency.

After space discretization a nonlinear differential algebraic system of equations is obtained where the unknowns are the discrete approximations to the continuous variables. For time-domain transient analysis, application of a suitable integration scheme leads to a system of nonlinear algebraic equations. Some device simulators use explicit integration methods so that the equations can be solved in a decoupled manner. Although explicit methods are computationally inexpensive, their stability properties make them unsuitable for simulations. Therefore implicit integration methods should be used to ensure reliable simulation results. The nonlinear algebraic equations obtained after integration, are linearized using the Newton-Raphson technique and solved by means of relaxation methods or direct methods.

2.4.2 Methods for Electromechanical Analysis

Although there are many microelectromechanical system (MEMS) designs that use piezoelectric, thermal, pneumatic, and magnetic actuation, the most popular approach is to use electrostatic forces to move the micromachined

structures. Electrostatically actuated microstructures are also referred to as electrostatic MEMS.

Typical micromachined structures are geometrically complicated and innately three-dimensional. In addition, the performance of these structures depends critically on exterior forces, like electrostatic pressure and fluid traction, in large or semi-infinite domains. Though it is possible to determine these forces by using finite-element or finite-difference discretization of the associated partial differential equations, such an approach has many difficulties. The most obvious problems in finite-element methods (FEM) are generating a well-behaved mesh (particularly if the structure is deforming), truncating the semi-infinite domain while still ensuring accuracy, and solving an unstructured sparse matrix with a large number of unknowns.

For many micromachined device applications, the exterior forces can be described by time-independent linear partial differential equations. For such problems, boundary-element methods (BEM) applied to surface-integral formulations can be used to avoid the exterior meshing and domain truncation problems. However, boundary element methods typically generate dense matrices and, therefore, sparsification and accelerated iterative methods are required to solve such matrices [9].

Computational analysis of electrostatic MEMS requires a self-consistent solution of the coupled mechanical and electrical equations. Conventionally, FEM is employed to perform the mechanical analysis and a BEM is employed to

compute the surface charge densities or the electrostatic pressure. However, FEM and BEM methods require mesh generation, mesh compatibility, re-meshing and interpolation between the domains. Mesh generation can be difficult and time consuming for complex geometries. Furthermore, mesh distortion can occur for micromechanical structures that undergo large deformations.

The difficulties in employing FEM/BEM for electromechanical analysis can be overcome by using a meshless finite cloud method (FCM) to solve the interior mechanical domain and a boundary cloud method (BCM) to analyze the exterior electrostatic domain [10]. FCM is a true meshless method in which only points are needed to cover the structural domain and no connectivity information among the points is required. This method completely eliminates the meshing process and radically simplifies the analysis procedure. BCM utilizes a meshless interpolation technique and a cell based integration. Besides the flexibility of the cell integration, BCM is an excellent match to FCM for coupled domain analysis since both of them have meshless interpolations. A Lagrangian description of the boundary integral equation is used to map the electrostatic analysis to the undeformed position of the conductors, thus eliminating the requirement of geometry updates and re-computation of the interpolating functions.

In this work the meshless methods, FCM and BCM have been used for electromechanical analysis due to their numerous advantages over FEM/BEM methods.

3 MEMS-BASED VARACTORS

3.1 Introduction

Modern wireless systems require high quality VCOs that exhibit wide tuning range and low phase noise. The tuning range should be wide enough to cover the desired frequency span over process and temperature variations. Frequency tunability in VCOs is normally provided by variable capacitors which are often implemented as external components. This is because of the difficulty in realizing high-Q factor on-chip variable capacitors. Integrated VCOs normally rely on p-n junction varactors for frequency tuning. However, in low phase-noise applications, the Q factor of an integrated p-n junction varactor is often inadequate and, hence, use of an alternative variable capacitor is necessary.

In recent years, MEMS technology is being used in wireless communication systems to improve the performance of existing devices. The advent of MEMS technology has made it possible to realize on chip variable capacitors with high-Q factors and wide tuning ranges [11]. In addition, MEMS variable capacitors can withstand large voltage swings, unlike a p-n junction varactor, where voltage swing must be limited to avoid placing the p-n junction in the forward bias region. These desirable characteristics of MEMS variable capacitors make them very suitable for low phase-noise VCO applications.

This chapter describes the working principle of MEMS variable capacitors. A functional model for a conventional MEMS variable capacitor and the equations governing its operation are described. Device characteristics and design considerations are illustrated. An overview of different configurations of the MEMS variable capacitor is presented. Parasitics associated with the MEMS capacitor are described and models for the different MEMS variable capacitor structures are presented. These models are necessary for the accurate simulation of VCOs employing MEMS variable capacitors for frequency tuning.

3.2 Working Principle

Fig. 3.1 shows a functional model of a conventional electro-mechanically tunable capacitor that consists of two parallel plates. The top plate of the capacitor is suspended by a spring and the bottom plate of the capacitor is fixed. When a bias voltage is applied across the capacitor plates, the suspended top plate is attracted towards the fixed bottom plate due to the resultant attractive electrostatic force. The top plate moves towards the bottom plate until equilibrium is reached between the attractive electrostatic force and the restoring spring force. Hence, upon equilibrium, the top plate experiences a displacement x due to an applied external voltage V. If the operation of the structure is limited to small deflections, as is the case for most

RF MEMS devices, the mechanical behavior can be modeled using a linear spring constant, k_m (N/m).

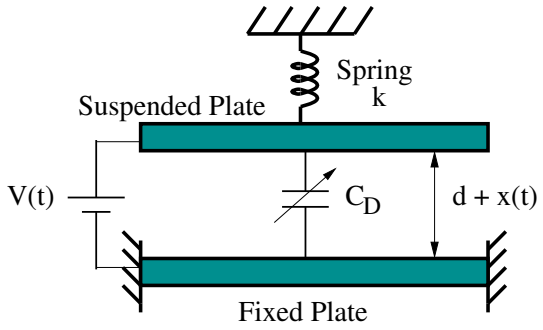

Fig. 3.1 Functional model of an electro-mechanically tunable parallel-plate capacitor.

Under dc conditions, $x(t) = x$, $V(t) = V$, and the desired capacitance is given by,

$$C_D = \frac{\varepsilon_0 A}{(d + x)} \tag{3.1}$$

The equilibrium between the forces can be expressed as (3.2) [11].

$$k_m x = \frac{1}{2}\frac{dC_D}{dx}V^2 = -\frac{1}{2}\frac{\varepsilon_0 A V^2}{(d + x)^2} \tag{3.2}$$

where, ϵ_0 is the dielectric constant of air, A is the area of the capacitor plates and d is separation of the capacitor plates when the spring is in its relaxed state. The voltage at which equilibrium is reached between the electrostatic and mechanical forces is referred to as the pull-in voltage, V_{PI}. Once the applied voltage exceeds the pull-in voltage, the top plate snaps down towards the substrate which is called the pull-in phenomenon. This phenomenon limits the tuning capacity of MEMS capacitors.

Using (3.2), it can be shown that the top plate can experience a maximum displacement equal to one-third the initial gap between the plates, i.e., $x_{max} = -d/3$, [11] where the negative sign represents displacement in the downward direction. Hence, the maximum capacitance tuning ratio that can be achieved from a conventional MEMS variable capacitor is 1.5:1. Substituting x_{max} in Eq. (3.2), an expression for the pull-in voltage can be obtained as given in Eq. (3.3).

$$V_{PI} = \sqrt{\frac{8k_m d^3}{27\varepsilon_0 A}} \tag{3.3}$$

From the above equation it can be seen that for a given nominal capacitance the pull-in voltage depends only on the spring constant, k_m. The nominal capacitance of the MEMS capacitor is the capacitance for zero applied voltage. Hence, for a given nominal capacitance, the initial gap, d, and the area of the top plate, A, are fixed.

3.3 MEMS Variable Capacitor Structures

Among all the MEMS variable capacitors developed to date, the electrostatically actuated parallel-plate configuration is the most commonly used. A parallel-plate variable capacitor can be fabricated easily using surface micromachining techniques. However, the theoretical tuning range of such capacitors is limited to 50% by the pull-in effect. The actual achieved tuning range is often much smaller than the theoretical value due to parasitic capacitances. Recently, different MEMS variable capacitor structures have been examined for improved tuning capability. However, expensive fabrications and measurements are required to study the effects of these structures on the performance of VCOs. The coupled simulator developed in this work can support different MEMS variable capacitor structures and can be effectively used to study MEMS VCOs without the need for expensive and time consuming fabrication processes.

Different MEMS capacitor structures have been simulated and their tuning characteristics are compared. These MEMS capacitors are manifestations of the same functional model as shown in Fig. 3.1. However, their structural differences result in varied tuning characteristics. The tuning characteristics are illustrated in the next chapter. In this section, an overview of the different MEMS capacitor structures used in this work is presented. Parasitics associated with these devices are described and design constraints are discussed.

3.3.1 Cantilever Beam and Fixed-Fixed Beam Capacitors

Cantilever beams and fixed-fixed beams are the simplest forms of electrostatically actuated MEMS-based capacitor structures. These structures and their deformation due to the application of an external bias voltage are shown in Fig. 3.2.

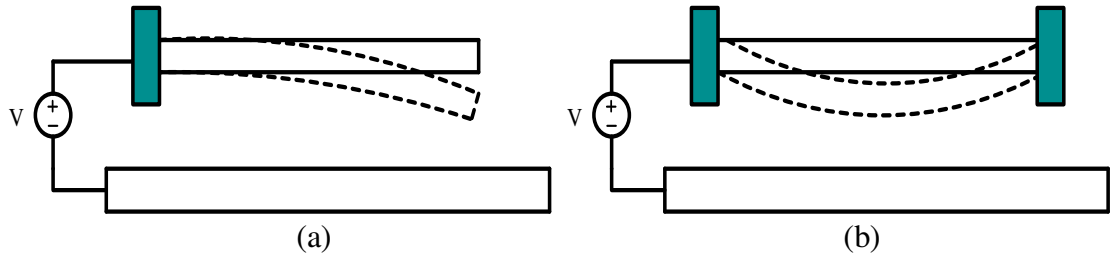

Fig. 3.2 (a) Cantilever beam and (b) fixed-fixed beam capacitor.

Cantilever beams are useful in many situations where it is inconvenient to fix both ends of the beam. The spring constant for a cantilever beam due to an uniform electrostatic force applied over the entire beam is given by [12]

$$k_m = \frac{2}{3} YW \left(\frac{t}{L} \right)^3 \tag{3.4}$$

where Y is the Young's modulus of the material of the beam, W is the width, t is the thickness, and L is the length of the beam.

Fixed-fixed beams are commonly used due to their relatively high spring constant and ease of manufacturing. The spring constant for a fixed-fixed beam can be expressed as (3.5) [12].

$$k_m = 32YW\left(\frac{t}{L}\right)^3 \tag{3.5}$$

From (3.2) and (3.3), it is clear that the spring constant k_m is an important design parameter. It determines the pull-in voltage and, therefore, the tuning range of the MEMS capacitor for a given nominal capacitance. However, in the case of cantilever beam capacitors and fixed-fixed beam capacitors, the spring constant is a function of the device dimensions and is therefore fixed for a given nominal capacitance. Thus, in the design of these capacitors, there is no degree of freedom to maximize the tuning range. In order to eliminate this constraint, additional suspension structures can be introduced which provide much more flexibility in the design of wide tuning range MEMS variable capacitors.

3.3.2 Two-Parallel-Plate MEMS Capacitor with Suspension Structures

Fig. 3.3 shows the top and cross-section views of a MEMS-based capacitor with mechanical suspension structures. These structures are shown as four arms protruding out of the top plate. The mechanical suspension design is a critical factor for MEMS variable capacitors. The suspension structures can be designed to

obtain the required stiffness constant and thus the desired tuning range. The spring constant for each arm is given by

$$k_s = YW_s\left(\frac{t_s}{L_s}\right)^3 \tag{3.6}$$

where W_s is the width, L_s is the length, and t_s is the thickness of each suspension structure [13]. The total mechanical spring constant for the structure, k_m, is the sum of the four suspension spring constants as expressed by (3.7).

$$k_m = 4k_s \tag{3.7}$$

From (3.6) and (3.7) it can be seen that the effective spring constant of the two-parallel-plate MEMS capacitor is linearly proportional to the beam width and highly dependent upon the beam length and thickness. Therefore, by varying the suspension dimension, different beam stiffness can be obtained for various tuning voltages.

The top plate parasitic capacitance, C_{TP}, and the bottom plate parasitic capacitance, C_{BP}, are shown in Fig. 3.3(b). The top plate parasitic capacitance, C_{TP}, between the suspension structures and the substrate appears in parallel with the desired variable capacitor. This not only reduces the tuning range, but can also lower the quality factor of the overall capacitor because C_{TP} suffers from the

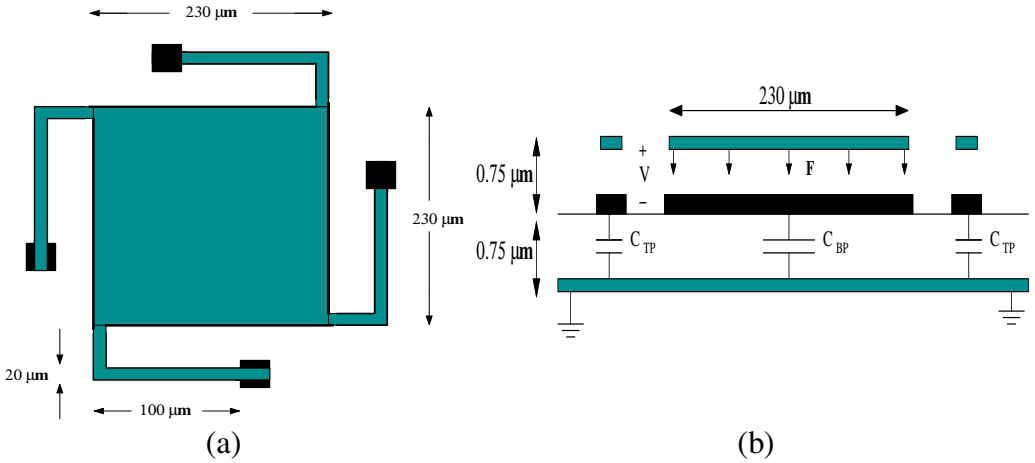

Fig. 3.3 (a) Top view and (b) cross-sectional view of the two-parallel-plate capacitor.

resistive substrate loss resulting in a low Q value [13]. The bottom plate parasitic capacitance, C_{BP}, between the bottom plate and the substrate has a lesser effect on the overall tuning range. In addition to introducing the top plate parasitic capacitance, the suspension structures are also the dominant contributors of series resistance, R_S, [11] which determines the Q of the device. In this work, the total series resistance of the MEMS capacitor is assumed to be entirely due to the suspension structures and is computed as

$$R_S = \frac{1}{4} R_{\square} \left(\frac{W_s}{L_s} \right) \tag{3.8}$$

where, $R_{\square}$ is the resistance per square of the material, and the factor of 4 is due to the four suspension arms.

From the above discussion it can be seen that the tuning range of MEMS variable capacitors can be increased by increasing the beam width of the suspension structures. However, an increase in the beam width also results in higher parasitic capacitances as well as a higher loss. Thus, a prudent design of the suspension structure is necessary such that these trade-offs are taken into account and an optimal performance is achieved from the MEMS variable capacitor.

3.3.3 Wide Tuning Range Three-Parallel-Plate MEMS Capacitor

A conceptual model of a novel, wide tuning range three-parallel-plate MEMS-based variable capacitor is shown in Fig. 3.4 [11]. The top and bottom plates of the capacitor are fixed mechanically and the middle plate is suspended by two springs with a spring constant $k_m/2$ each. Under zero bias condition the distances between the parallel plates are d_1 and d_2 respectively as shown in Fig. 3.4.

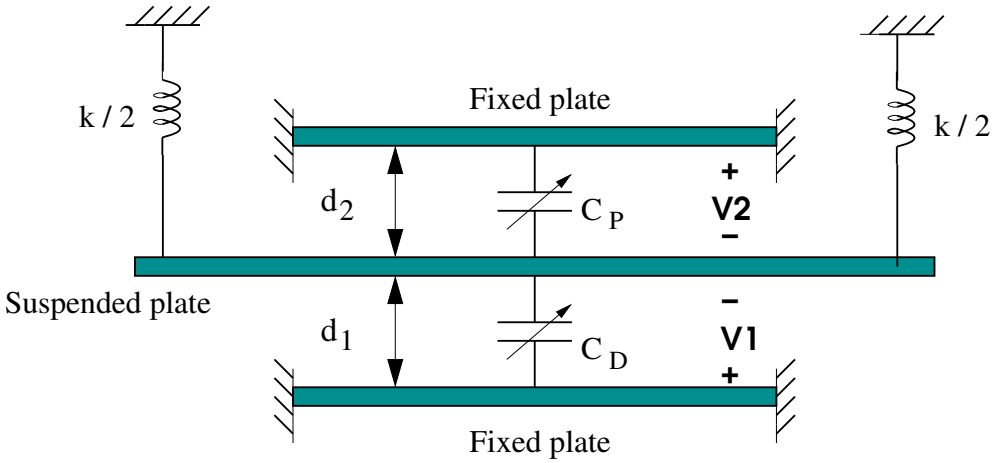

Fig. 3.4. Wide tuning range three-parallel-plate capacitor.

This three-plate MEMS variable capacitor structure operates in a dual mode with two applied voltages. If a bias voltage V_1 is applied and V_2 = 0 V, the electrostatic force causes the suspended plate to move towards the bottom plate. Similarly, if a bias voltage V_2 is applied and V_1 = 0 V, the suspended plate moves towards the top plate. Under dc conditions, the equilibrium between the electrostatic force and restoring spring force can be expressed as

$$\begin{aligned} k_m x &= \frac{1}{2}\frac{dC_D}{dx}V_1^2 + \frac{1}{2}\frac{dC_P}{dx}V_2^2 \\ &= -\frac{1}{2}\frac{\varepsilon_0 A V_1^2}{(d_1+x)^2} + \frac{1}{2}\frac{\varepsilon_0 A V_2^2}{(d_2-x)^2} \end{aligned} \tag{3.9}$$

As in the two-parallel-plate case, the maximum capacitance that can be obtained is still $3C_D/2$. However, the minimum capacitance that this capacitor can be tuned to is $3C_D/4$, assuming d_1 and d_2 are equal. Hence, the maximum theoretical tuning range that can be obtained from this MEMS variable capacitor structure is 2:1 [11].

The springs are realized by suspension structures in this case as well. Therefore, the desired capacitance is accompanied by the same parasitics due to the suspension structures as discussed for the two-parallel-plate case. In addition to these parasitics, a voltage dependent parasitic capacitance C_P is inherently associated with the device. The effect of this capacitance on the frequency tuning characteristics of the VCO is discussed in the next chapter.

3.4 Lumped Equivalent Models for MEMS Capacitors

An efficient method of simulating a system consisting of different physical domains is by the use of lumped element equivalent circuits. In the case of MEMS-based capacitors, the displacement of the top plate in the mechanical domain can be represented by an equivalent capacitance in the electrical domain. In addition, the desired capacitance of the MEMS capacitor is always accompanied by some parasitics which were described in the previous section. These device parasitics consist of the top and bottom plate parasitic capacitances as well as the series resistance.

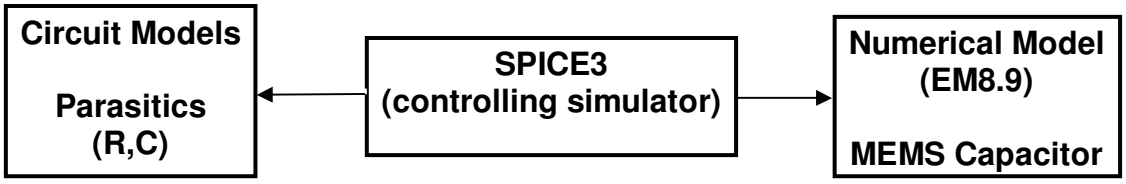

Fig. 3.5. Modeling the MEMS capacitor in the coupled simulation environment.

In this work, the numerical solution of device level equations is used to accurately compute the displacement and, therefore, the capacitance of the MEMS capacitor. The device solver that has been employed for numerical analysis of the MEMS capacitor is an electrostatic MEMS simulator called EM8.9 [10]. A brief description of this simulator is provided in the next chapter. As shown in Fig. 3.5

the actual MEMS capacitor is represented by a numerical device model, while the associated device parasitics are represented by their equivalent circuit models. Furthermore, since SPICE3 is being used as the controlling simulator, it has access to both the numerical model as well as the circuit models. Hence, this SPICE3-EM8.9 coupled simulation environment is used to accurately model the MEMS capacitor along with its associated parasitics.

The two-parallel-plate MEMS-based capacitors are modeled as two-terminal devices as shown in Fig. 3.6. The top plate parasitic capacitance C_{TP}, the bottom plate parasitic capacitance C_{BP} and the series resistance R_S are independent of the applied voltage. Therefore, their values can be easily calculated and included in the circuit. In order to eliminate the extra node created due to the series

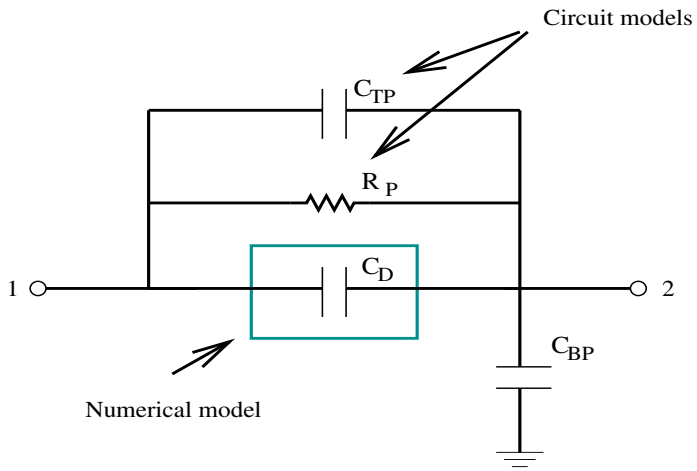

Fig. 3.6. Lumped element model for the two-parallel-plate MEMS capacitor.

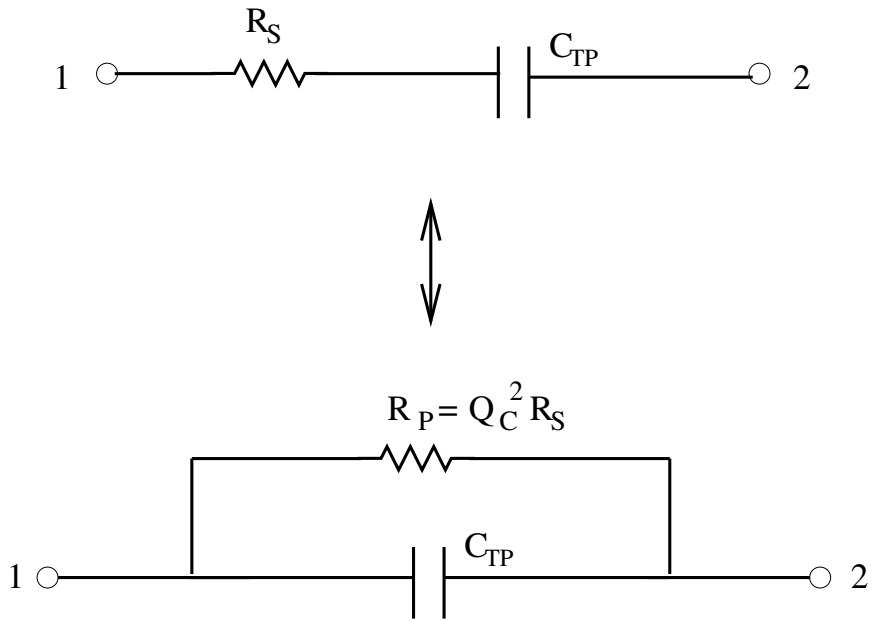

Fig. 3.7. Series-to-parallel transformation.

resistance, its parallel equivalent, R_P, is used. Assuming that the quality factor, Q_C, is sufficiently high, the series-to-parallel transformation is as shown in Fig. 3.9 [14]. Since the cantilever and fixed-fixed beams do not have any suspension structures, the parasitic capacitance and series resistance were not included in their lumped models. The wide tuning range, three-parallel-plate MEMS-based capacitor was modeled as a three terminal device as shown in Fig. 3.8. Since the parasitic capacitance C_P is a function of the applied voltage V_2, it is evaluated by the model along with the desired capacitance C_D. The calculated top plate parasitic capacitance and the parallel equivalent of the series resistance are added in parallel to the MEMS capacitor.

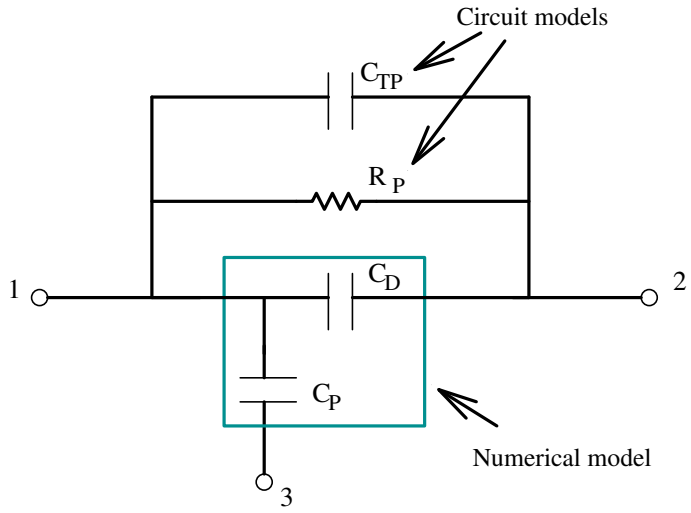

Fig. 3.8. Lumped element model for the three-parallel-plate MEMS capacitor.

3.5 Dynamic Characteristics

The dynamic behavior of MEMS variable capacitors can be modeled as a mass-spring-damper system as illustrated in Fig. 3.9. The displacement of the top plate of the capacitor, *x*, can be described by a second order differential equation as given by [12]

$$m\frac{d^2x(t)}{dt^2} + b\frac{dx(t)}{dt} + k_m x(t) = F_e \tag{3.10}$$

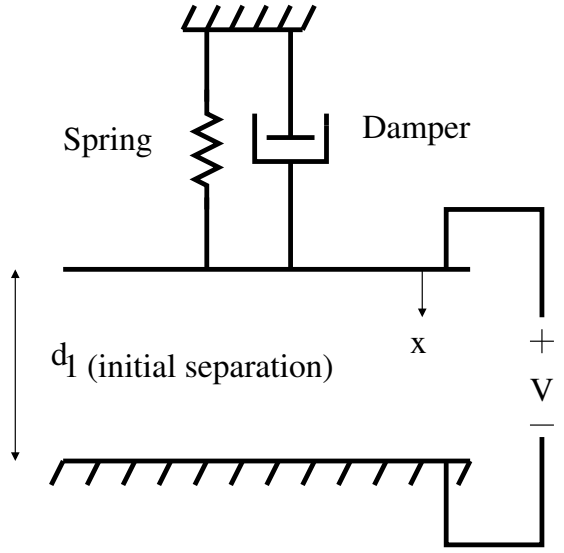

Fig. 3.9. Mass-spring-damper model of the MEMS capacitor.

where, m is the mass of the top plate of the MEMS capacitor, b is the damping coefficient due to the surrounding gas ambient and the internal dissipation of the system and F_e is the attractive electrostatic force. Since (3.10) is linear, it can be transformed into the Laplace domain and the frequency response of the system can be obtained. Fig. 3.10 illustrates a linear system equivalent representation of the MEMS variable capacitor in the s-domain where $H(s)$ is the impulse response of the system.

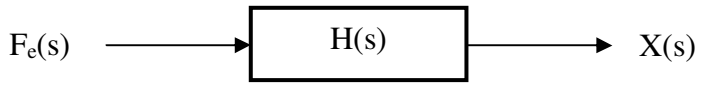

Fig. 3.10. Linear system representation of the MEMS variable capacitor.

By transforming (3.10) into the Laplace domain , *H(s)* can be obtained as given by

$$H(s) = \frac{X(s)}{F(s)} = \frac{1}{ms^2 + bs + k_m} = \frac{1/m}{s^2 + \frac{\omega_n}{Q_M}s + \omega_n^2} \tag{3.11}$$

where $\omega_n = \sqrt{k_m / m}$ is the mechanical resonant frequency of the micromachined structure and $Q_M = (\omega_n m)/b$ is the mechanical quality factor. Inspection of (3.11) reveals that *H(s)* has a second order low-pass response with the 3-dB cut-off frequency corresponding to the mechanical resonant frequency ω_n and dc gain equal to $1/k_m$. The magnitude frequency response of *H(s)* is shown in Fig. 3.11 for a typical design condition (ω_n = 30 kHz, k_m = 3.4 N/m, Q_M = 1). It can be seen that at resonance, the displacement is amplified by a factor of Q_M, resulting in peaks and the response drops at 40 dB per decade for frequencies higher than ω_n.

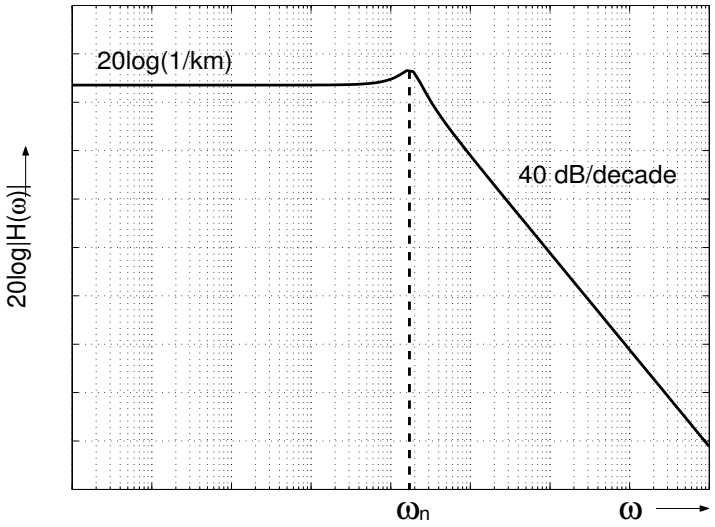

Fig. 3.11. Frequency response of the input force to displacement transfer function.

The low-pass nature of the frequency response reveals that the displacement of the top plate, and therefore, the capacitance of the MEMS-based capacitor varies only for low frequency excitations and remains unchanged for input frequencies higher than ω_n. Since the RF frequency of interest is almost six orders of magnitude larger than the mechanical resonant frequency the variable capacitor is independent of RF signals. This characteristic results in an extremely linear behavior and makes MEMS variable capacitors attractive for low distortion applications.

4 COSMO: COUPLED SIMULATOR FOR MEMS OSCILLATOR

4.1 Introduction

Coupled circuit and device simulations are extremely beneficial for the study of microelectromechanical systems. A coupled simulator can facilitate accurate simulations of these systems even in the absence of proper macromodels for the MEMS devices. Different devices can be simulated using physics-based numerical models when there are stringent accuracy requirements on simulated results. The behavior of different device structures can also be analyzed without having to construct a macromodel for each structure.

Recently, different configurations of the MEMS-based capacitor have been examined for improved tuning range. In addition to having a high Q factor and a wide tuning range, MEMS variable capacitors can also withstand large voltage swings, thus making them suitable for low phase noise VCO applications. However, the absence of an accurate model for the MEMS variable capacitor has made it difficult to simulate the behavior of MEMS VCOs. This results in an extremely long design cycle or conservative design practices. As a possible solution to these problems, a coupled circuit and device simulator for the improved design of MEMS-

capacitor based RF VCOs, COSMO, is presented. COSMO is an integration of the circuit simulator, SPICE3f5, with an electrostatic/mechanical simulator.

Coupled simulations can efficiently simulate the tuning characteristics and phase noise in RF MEMS VCOs. Comparisons between simulated results and existing experimental data demonstrate the accuracy of this approach. The working principle of MEMS variable capacitors was described in the previous chapter. It was seen that in order to fully comprehend the nature of MEMS variable capacitors, it is important to study their behavior for both static and dynamic conditions. In this chapter, a method for the accurate computation of the capacitance of a MEMS capacitor is presented. A detailed coupling description of COSMO which is designed for accurate static as well as dynamic simulations of MEMS variable capacitors is described. Furthermore, important simulation issues such as convergence and time-stepping are also described. The effects of different MEMS capacitor structures and materials on the tuning characteristics of the VCO are illustrated and comparisons with experimentally observed behavior are presented. Simulation of phase noise in RF MEMS VCOs is discussed in detail in the next chapter.

4.2 Device Simulations and Capacitance Computation

COSMO is an integration of the circuit simulator SPICE3f5 with a device simulator EM8.9. EM8.9 is a numerical solver for electrostatic MEMS analysis using a meshless method [10]. It employs the finite cloud method (FCM) for mechanical analysis and the boundary cloud method (BCM) for electrostatic analysis. FCM and BCM methods obviate the need for complicated and time consuming mesh generation. Lagrangian descriptions are used to map the electrostatic analysis to the undeformed geometry of conductors, thus eliminating the need for geometry updates and re-computation of the interpolation functions. The procedure for the self-consistent analysis of coupled electromechanical devices in EM8.9 can be summarized as follows. Electrostatic analysis using BCM is done first to compute the surface charge density and the electrostatic pressure, which is then used in the mechanical analysis (performed on the undeformed geometry by FCM) to compute the structural displacement. This procedure is repeated until a state of equilibrium is achieved.

As described above, EM8.9 solves for the structural displacement of the MEMS capacitors for a given applied voltage. This solution obtained from EM8.9 is used to compute the capacitance of the MEMS capacitor. The input to EM8.9 is specified in the form of the applied voltages, dimensions, geometry, number of

discrete nodes and the material properties. A set of these input parameters defines a unique problem which is processed by EM8.9 in three phases.

The first phase is the *initialize* phase which involves reading in the input, discretization, generating nodes and memory allocation. The second phase is the *solve* phase where the structural displacement of each discrete element is computed along both the x-axis and the y-axis and stored in the two-dimensional displacement vectors *xdisp* and *ydisp*. Finally, in the *update* phase the geometry and displacement vectors are updated. The *solve* and *update* phases are repeated until convergence.

The capacitance is computed after the *solve* phase upon convergence. Since the displacement along the *x-axis* is small and assuming a sufficiently large number of nodes, each discrete element can be treated as a parallel-plate capacitor (Fig. 4.1)

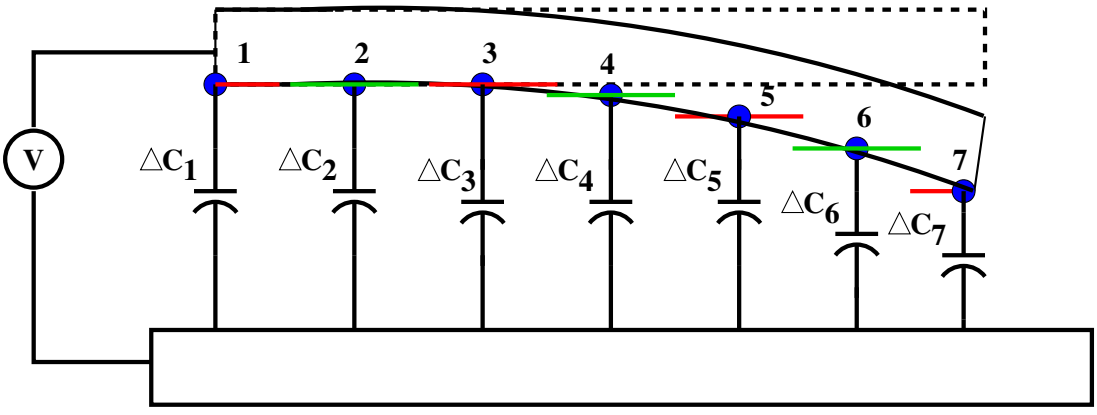

Fig. 4.1. Capacitance computation of the MEMS capacitor.

and the incremental capacitance between each element and the bottom plate can be computed. Finally, the total capacitance of the MEMS capacitor can be computed by adding all the incremental capacitances and is given by

$$C_{MEMS} = \frac{\varepsilon_0 A}{2(N-1)}\left(\frac{1}{d_1} + 2\sum_{j=2}^{N-1}\frac{1}{d_j} + \frac{1}{d_N}\right) \tag{4.1}$$

$$d_j = g_0 - ydisp(1, j) \tag{4.2}$$

where, ϵ_0 = permittivity of air,

A = area of the top plate,

N = number of discrete nodes along the length of the top plate,

g_0 = gap between the two plates for a zero applied voltage, and

ydisp (i, j) = vertical displacement of the j^{th} node along the length of the i^{th} surface of the top plate. (i = 1 corresponds to the bottom surface)

This method is used to compute the capacitance of the MEMS capacitor for different applied voltages. The capacitance as a function of voltage for a simple cantilever beam capacitor is as shown in Fig. 4.2. It is seen that the capacitance is symmetric about the y-axis owing to the attractive nature of the electrostatic force for both positive and negative applied voltages. The accuracy of the capacitance

computation method is easily validated by comparing the nominal capacitance with the capacitance computed for a zero applied voltage. The device becomes unstable once the applied voltage exceeds the pull-in voltage and results in an arbitrary change in the capacitance value as shown in Fig. 4.2. This necessitates a suitable voltage-limiting scheme to ensure convergence in EM8.9.

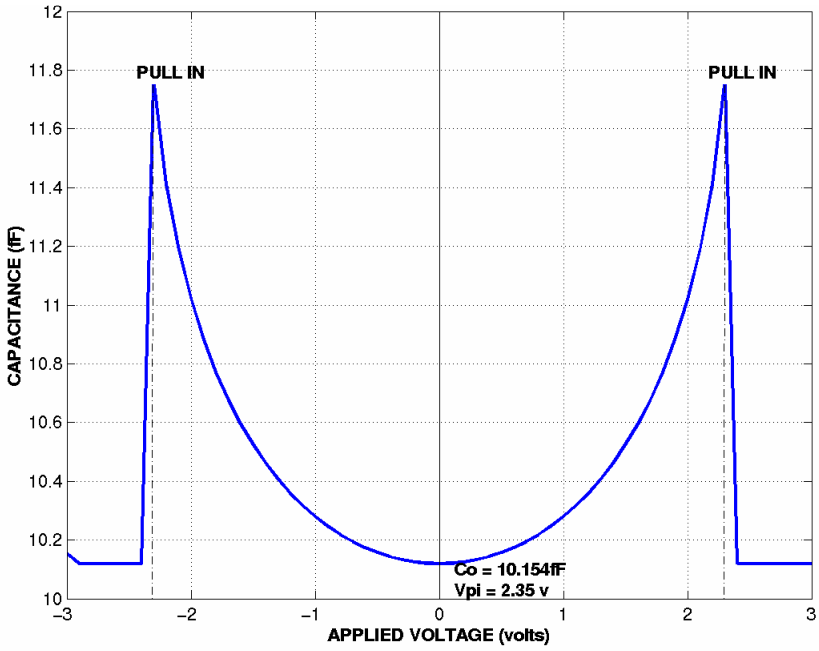

Fig. 4.2. Computed capacitance as a function of voltage for a MEMS capacitor.

4.3 Coupling Description for Static Simulations

SPICE3f5 and EM8.9 are integrated for static simulations by using file processing and system calls. SPICE3 treats the MEMS capacitor device as a numerical model as discussed in Section 3.4. A block diagram illustrating the coupling between the two simulators is shown in Fig. 4.3. At every Newton iteration, SPICE3 computes the node voltages required by EM8.9 for numerical model evaluation. Then SPICE3 calls EM8.9 using the system command and passes the bias voltages and dimensions of the MEMS capacitor through data files. In response to the call, EM8.9 computes the capacitances using the method described in the previous section and returns the capacitance value back to SPICE3 through another data file. After retrieving the necessary data, SPICE3 loads the capacitance value and updates the Jacobian matrix and the RHS vector. Finally, the equations are solved to obtain the new node voltages and the process repeats.

When the applied voltage across the MEMS capacitor exceeds the pull-in voltage, the device is unstable and hence the simulator does not converge. Therefore, a suitable voltage limiting scheme is used to avoid unnecessary device calls and, hence, reduce the computational cost. An estimate of the pull-in voltage of the MEMS capacitor can be obtained from (3.3) for a particular design condition. If the voltage across the MEMS capacitor is within a predefined range, *PULLTOL*, of the predicted pull-in voltage, the old value of the capacitance is loaded thus avoiding

a device call and preventing convergence problems. A more accurate value of the pull-in voltage can also be determined by simulating the device for various applied voltages using EM8.9.

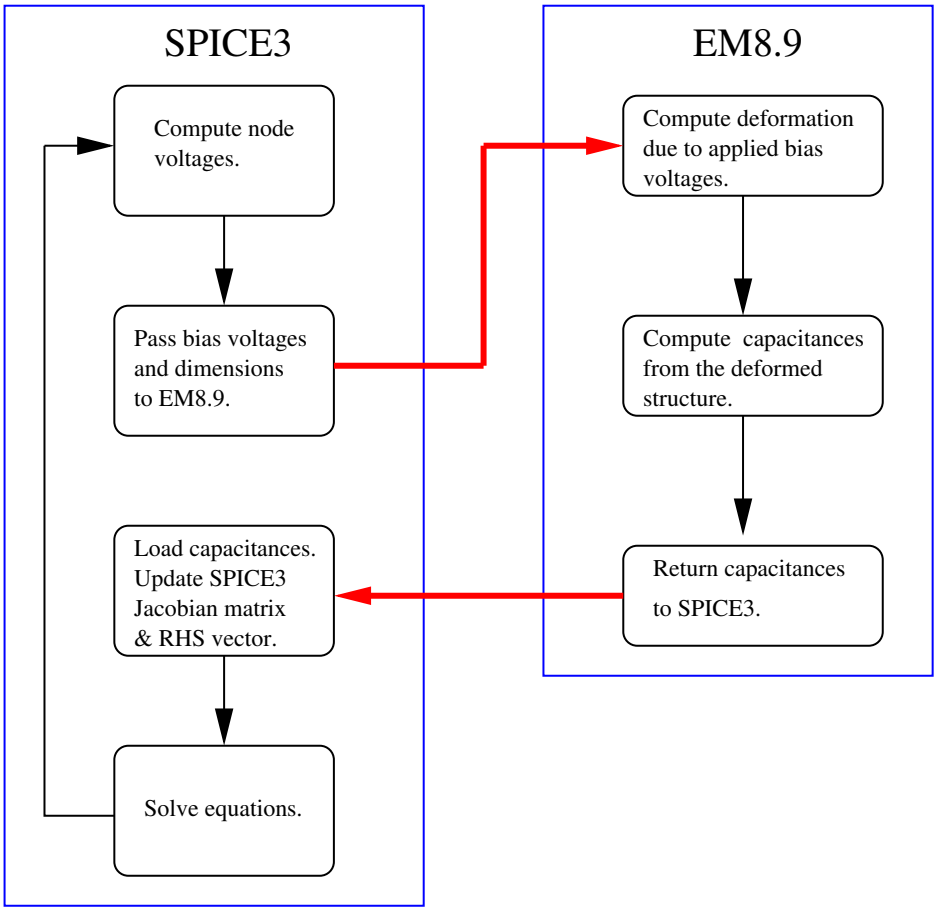

Fig. 4.3. The COSMO simulator showing coupling between SPICE3 and EM8.9.

4.4 Coupling Description for Dynamic Simulations

In the case of static simulations, the capacitance of the MEMS capacitor was only dependent on the instantaneous voltage across it. Therefore, SPICE3 and EM8.9 could easily communicate through data files with EM8.9 being reset after each device call. However, in the case of dynamic simulations, the capacitance of the MEMS capacitor depends on the past capacitance values in addition to the applied voltage. Therefore, it is difficult to use file processing in this case since EM8.9 needs to retain past history. As an alternative, EM8.9 is embedded in SPICE3 in the form of a subroutine for dynamic simulations. This closed form of coupling is used in COSMO for dynamic simulations.

An important issue in coupling circuit and device simulators for dynamic simulations is the control of time steps [6]. A transient analysis in SPICE3 results in nonuniform time steps and several Newton iterations for each time step. Typically, the time constants associated with circuits are of the order of 10^{-12} s to 10^{-6} s. On the other hand, MEMS capacitors have a typical time constant of the order of 10^{-6} s to 10^{-3} s. Hence, the time step used in EM8.9 is significantly larger than that used in SPICE3, and calling the device at each circuit time point would be computationally expensive. A computationally efficient alternative is to call the device after every several hundred circuit time steps or at every device time-step. In order to implement such a scheme an efficient time-stepping algorithm is employed. The time stepping scheme is as shown in Fig. 4.4.

In Fig. 4.4, time is plotted on the horizontal axis and SPICE3 Newton iterations are plotted on the vertical axis. T_{Ci} represents the i^{th} SPICE3 time point and T_{Dj} represents the j^{th} EM8.9 time point. $C_{m,n}$ corresponds to the capacitance value obtained at m^{th} EM8.9 time-point and n^{th} SPICE3 iteration and *EM_TSTEP* is the device time step. Each solid square corresponds to a device call and, therefore, carries a unique capacitance value. Since EM8.9 uses an explicit method for its transient analysis, device calls are made at every SPICE3 iteration. The circles represent no call to the device and hence retain the capacitance value obtained from the last device call. Due to the non-uniform time steps from SPICE3, synchronizing SPICE3 time points to EM8.9 time points is not straight forward. Therefore, appropriate breakpoints are generated during the circuit transient analysis to ensure that SPICE3 generates time points at every integer multiple of *EM_TSTEP*.

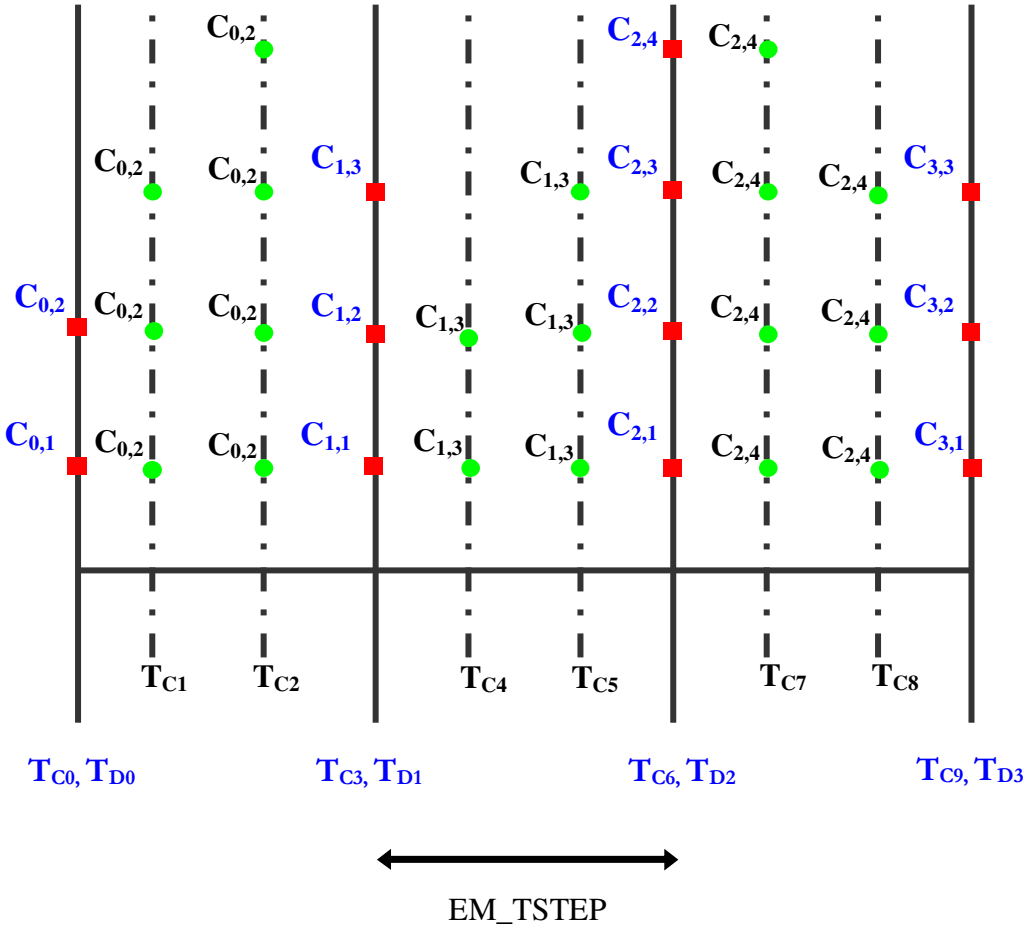

Fig. 4.4. The time stepping scheme used in COSMO for dynamic simulations.

4.5. MEMS VCO Circuit for Simulation of Tuning Characteristics

A 2.4 GHz LC cross-coupled VCO [15] implemented in a HP 0.5-µm CMOS technology is simulated to verify the tuning characteristics. The schematic of the VCO circuit is shown in Fig. 4.5. The cross-coupled pair (*M1*, *M2*) realizes the transconductance amplifier. The bias current is provided by the current mirror (*Mb1* and *Mb2*) using an ideal current source IBIAS. The resonant circuit of the VCO consists of two variable capacitors (C_D) and bond wire inductors (*Lb*) that are coupled together by mutual inductance (*M*).

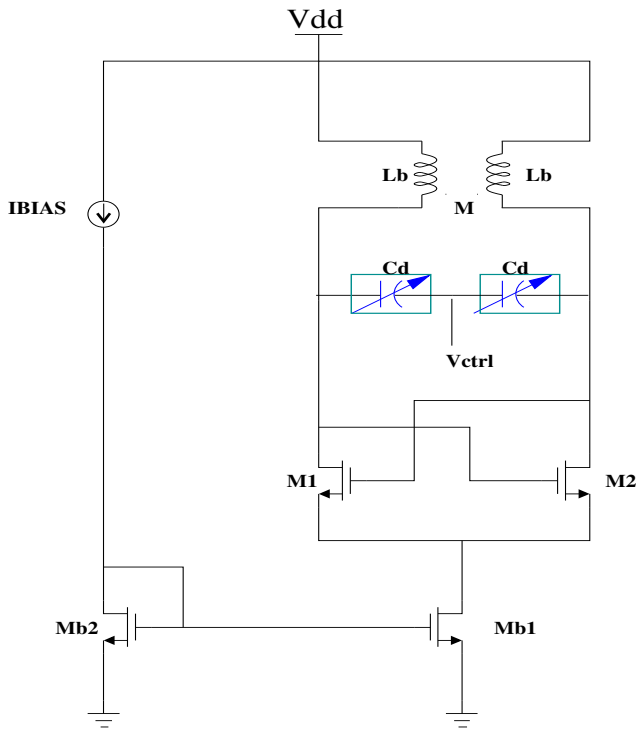

Fig. 4.5. VCO circuit for simulation of tuning characteristics.

The oscillation frequency of 2.4 GHz can be achieved by using a 1.4 pF MEMS variable capacitor and 2.2 nH bond wire inductors with a mutual inductance of 0.6 nH. The inductor has a *Q* factor of 117 at 2.4 GHz. The minimum required transconductance to ensure oscillation build up is 2.2 mS. However, the transconductance is conservatively chosen to be approximately 27 mS. The VCO consumes 5 mA of current, while operating from a 2.7 V power supply.

Different MEMS capacitor structures are simulated and their tuning characteristics are compared. An overlap area of 230 µm x 230 µm and an air gap of 0.75 µm are used for all the structures which results in a nominal capacitance of 0.624 pF. In order to maintain consistency with experimental results, pad parasitic capacitances of 750 fF are added in parallel to the MEMS capacitor. The suspension structures are designed to obtain a capacitance tuning ratio of 1.5:1 with a tuning voltage of 3.3 V.

4.6. Static Simulation Results and Validation with Experimental Data

The VCO circuit described above is simulated using COSMO. Three different MEMS variable capacitor structures are employed and their tuning characteristics are compared. The working principle of these MEMS capacitor structures and their design considerations were discussed in Section 3.3. Simulation

results are also illustrated for different materials of the two-parallel-plate capacitor structure.

4.6.1. Simulated Tuning Characteristics of Cantilever Beam and Fixed-Fixed Beam Capacitors

The capacitance tuning characteristics of the cantilever beam and fixed-fixed beam capacitors are as shown in Fig. 4.6. The cantilever beam capacitor shows a capacitance tuning ratio of 1.18:1 with a tuning voltage of 1.6 V while the fixed-fixed beam shows a capacitance tuning ratio of 1.27:1 with a tuning voltage of 10.5 V. As discussed in Section 3.3.1, cantilever beam and fixed-fixed beam capacitors lack an additional degree of freedom for their design. Hence, the designer does not have control over the tuning range of these structures for a fixed nominal capacitance. This results in widely varying tuning performances for the cantilever beam and fixed-fixed beam capacitors as seen in Fig. 4.6.

The simulated frequency tuning characteristics of the VCO employing cantilever beam capacitors and fixed-fixed beam capacitors are illustrated in Fig. 4.7. The cantilever beam capacitor shows a frequency tuning range of only 6.4% while the fixed-fixed beam capacitor offers a mere 0.6% tuning range with a tuning voltage of 2.7 V. Cantilever beams have low stiffness constants which results in small deflections of the top plate at low pull-in voltages and therefore these capacitor structures exhibit poor tuning characteristics [12]. On the other hand, fixed-fixed beams are highly non-linear with higher stiffness constants and,

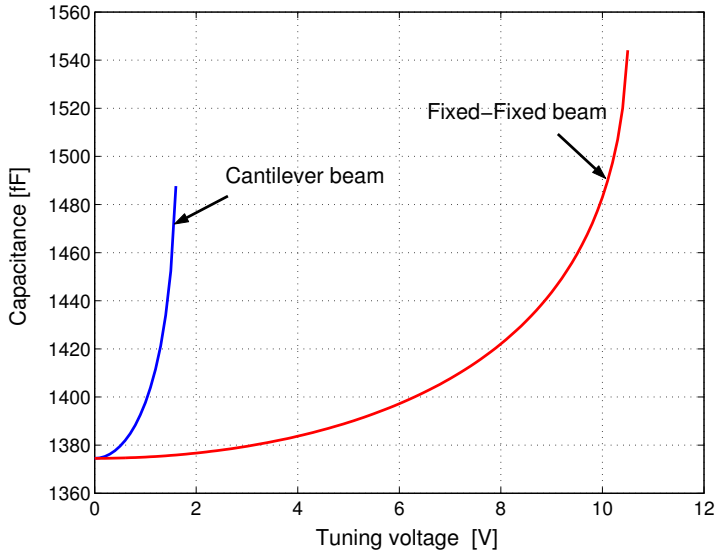

Fig. 4.6. Capacitance as a function of voltage for cantilever beam capacitors and fixed-fixed beam capacitors.

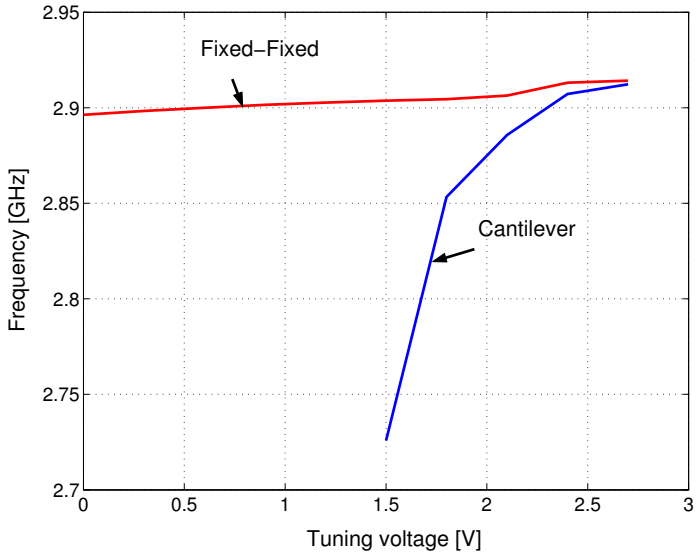

Fig. 4.7. Frequency as a function of voltage for cantilever beam capacitors and fixed-fixed beam capacitors.

therefore, have high pull-in voltages [12]. However, the non-linear behavior of fixed-fixed beams and the high tuning voltage requirements make them unsuitable for low voltage applications. It is seen from Figs. 4.6 and 4.7 that simulated results are in agreement with this theory.

4.6.2. Simulated Tuning Characteristics of the Two-Parallel-Plate Capacitor

COSMO is used to simulate two-parallel-plate capacitors for different thicknesses of the top plate as well as for different materials. The simulated results are validated with existing experimental data that have been presented in [15] for the 2.4 GHz VCO (Fig. 4.5) employing a two-parallel-plate MEMS variable capacitor.

The magnified version of the capacitance tuning characteristics for three different thicknesses is shown in Fig. 4.8. Since the top plate is non-rigid, it contributes to the overall stiffness constant of the MEMS capacitor. Hence, varying the thickness of the top plate alters the overall stiffness constant and therefore the tuning characteristic changes [16].

The two-parallel-plate capacitor is also simulated for three different materials, polysilicon/gold, aluminum, and nickel/gold for the same structural dimensions. Table 4.1 provides the values of the various design parameters and parasitics used for the three materials. It can be seen that polysilicon/gold has the highest stiffness constant while aluminum offers the highest Q factor. The top plate parasitic capacitance, C_{TP}, is calculated to be 32 fF and the bottom plate parasitic

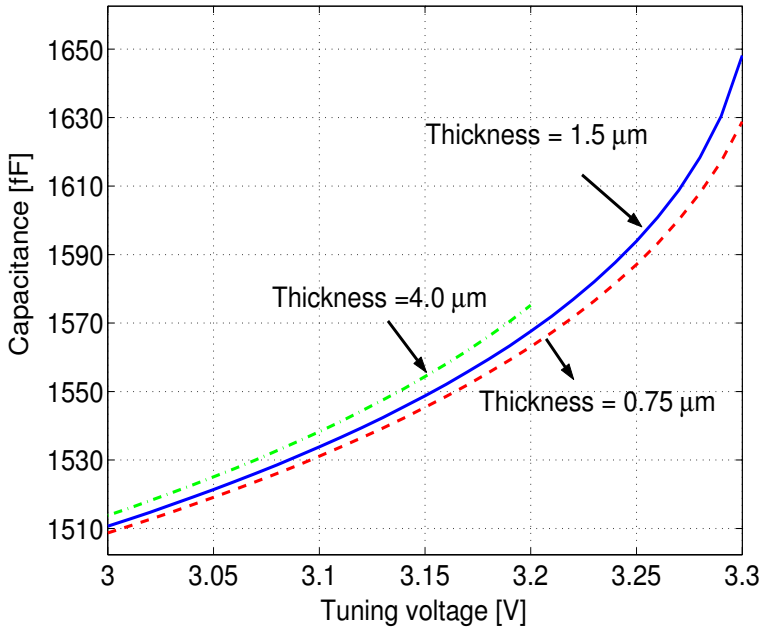

Fig. 4.8. Capacitance as a function of voltage for different thicknesses of the top plate.

TABLE 4.1. Design parameters and parasitics for different materials.

Material	Stiffness constant	Pull-in voltage	R_S	Q-factor at 2.4 GHz	R_P
Poly/Gold	44 N/m	3.3 V	5 Ω	9	400 Ω
Aluminum	18 N/m	2.1 V	1.2 Ω	40	1900 Ω
Nickel/Gold	52 N/m	3.5 V	5 Ω	9	400 Ω

capacitance, C_{BP}, is calculated to be 700 fF. Since the same dimensions are used for the three materials, there is no change in the values of C_{TP} and C_{BP}.

The capacitance tuning characteristics of the two-parallel-plate capacitors is as shown in Fig. 4.9. Simulations show that the polysilicon/gold structure offers the highest capacitance tuning ratio of 1.43:1 with a tuning voltage of 3.3 V. The aluminum and nickel/gold structures show capacitance tuning ratios of 1.37:1 and 1.32:1, respectively. The low capacitance tuning ratio of the aluminum structure can be attributed to its low pull-in voltage. On the other hand the capacitance tuning ratio in the nickel/gold structure is limited by the high stiffness constant.

The frequency tuning characteristics of the VCO employing the two-parallel-plate capacitor is illustrated in Fig. 4.10. Since the VCO operates with a power supply of 2.7 V, the tuning voltage is limited to only 2.7 V although the pull-in voltages are higher. The aluminum structure offers the highest frequency tuning range of 19.2%. The polysilicon/gold structure offers a tuning range of 14.6% while nickel/gold offers 7.3% tuning. This trend in the frequency tuning range can be explained by observing the maximum capacitance that can be achieved for each material for a tuning voltage of 2.7 V. From Fig. 4.9, it is clearly seen that aluminum offers the highest capacitance tuning ratio for a tuning voltage of 2.7 V.

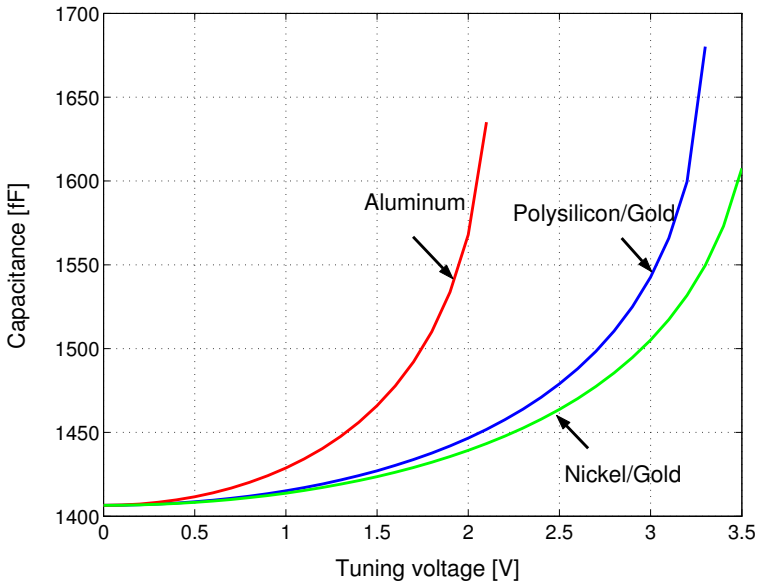

Fig. 4.9. Capacitance as a function of voltage for the two-parallel-plate capacitor.

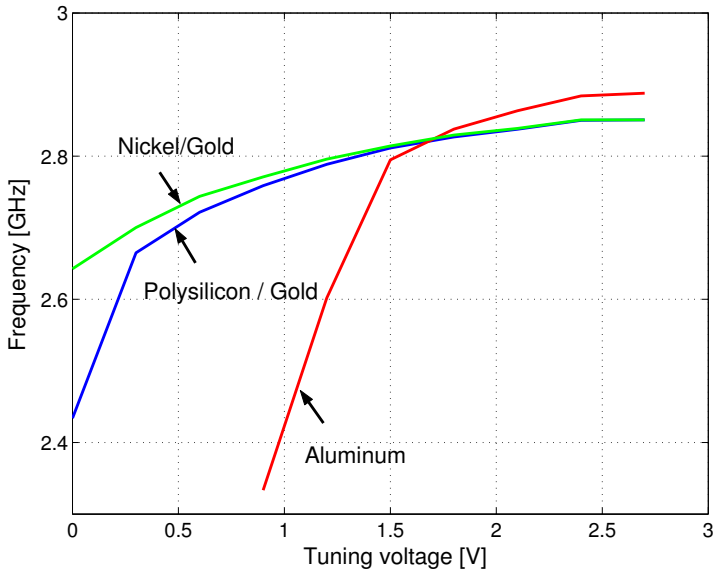

Fig. 4.10. Frequency as a function of voltage for the two-parallel-plate capacitor.

4.6.3. Simulated Tuning Characteristics of the Three-Parallel-Plate Capacitor

The three-parallel-plate MEMS variable capacitor was also simulated using COSMO. As described in Section 3.3.3, this structure consists of three plates where the middle plate is suspended and the top and bottom plates are fixed. The same suspension structure that was used for the two-parallel-plate polysilicon/gold capacitor is employed for this structure as well. Hence, the design parameters and parasitics remain the same, i.e., a stiffness constant of 44 N/m is used which results in a pull-in voltage of 3.3 V and the top plate parasitic capacitance is calculated to be 32 fF. From Fig. 3.4, it can be seen that a bottom plate parasitic capacitance does not exist for this structure. Instead, an inherent parasitic capacitance, C_P, accompanies the actual capacitance and is evaluated by EM8.9.

The capacitance tuning characteristics of the three-parallel-plate capacitor is shown in Fig. 4.11 for the two operating modes. The capacitance increases with an increase in the tuning voltage, V_B, for one mode (V_1=V_B, V_2=0) and decreases with an increase in V_B for the second mode (V_1=0, V_2=V_B). The capacitance tuning ratio obtained for the first mode is 1.44:1 and that obtained for the second mode in 1.31:1, therefore, resulting in an overall capacitance tuning ratio of 1.88:1 for a tuning voltage of 3.3 V. Fig. 4.12 shows the frequency tuning characteristics of the VCO employing the three-parallel-plate capacitor. Frequency tuning is shown for both modes of operation. The frequency is tuned from 2871 MHz to 2782 MHz in the first mode and from 2329 MHz to 2871 MHz in the second mode. Thus, a frequency tuning range of 23.28% is obtained from the three-parallel-plate structure

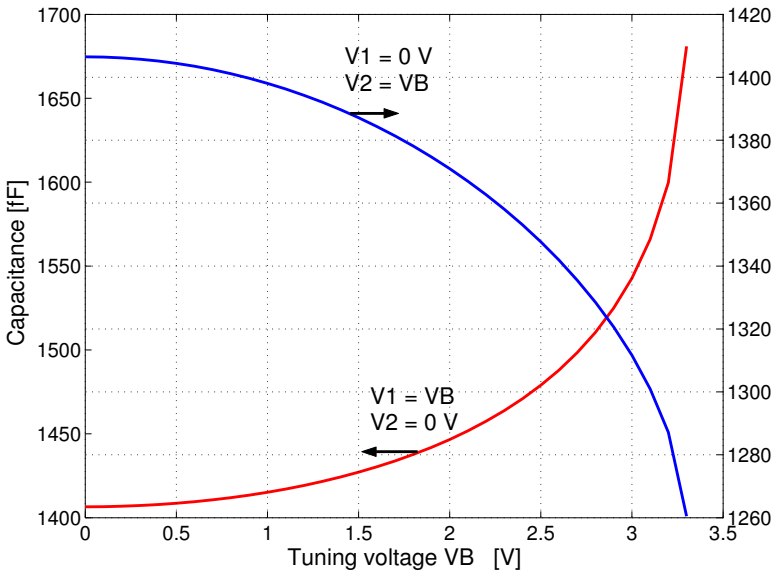

Fig. 4.11. Capacitance as a function of voltage for the three-parallel-plate capacitor.

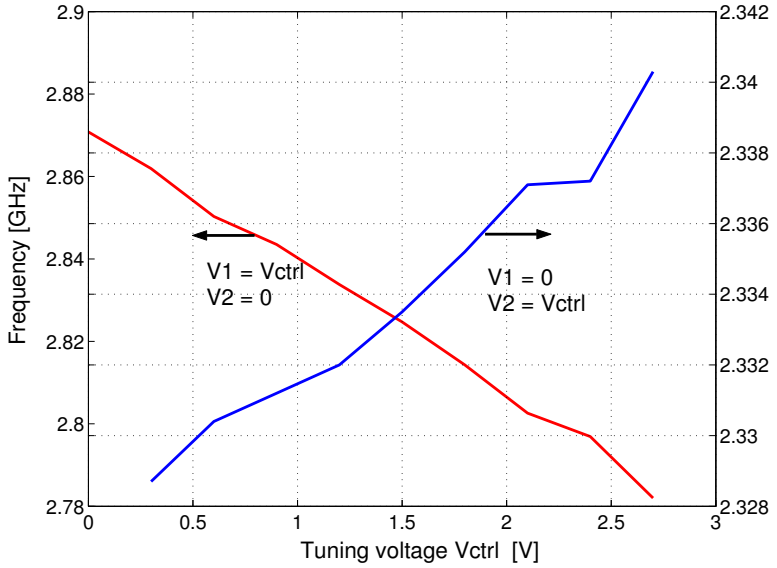

Fig. 4.12. Frequency as a function of voltage for the three-parallel-plate capacitor.

with a tuning voltage of 2.7 V. It should be noted that although this structure provides a high capacitance tuning ratio, the frequency tuning does not follow similar trends. This can be attributed to the inherent voltage dependent parasitic capacitance, C_P, which always accompanies the desired tunable capacitance. Another drawback of this structure is that the center frequency (in this case 2.6 GHz) does not appear in the frequency tuning characteristics. This is again due to C_P, which alters the frequency of oscillation for a zero applied voltage across the MEMS capacitor, and, therefore, the centre frequency is different from 2.6 GHz.

4.6.4. Summary and Comparisons

The tuning performance of the different MEMS variable capacitor structures is summarized in Table 4.2. It is seen that the cantilever beam and fixed-fixed beam capacitors exhibit a poor tuning performance. Among the two-parallel-plate MEMS variable capacitor structures, polysilicon/gold offers the highest capacitance tuning ratio while aluminum provides the highest frequency tuning range. Finally, although the three-parallel-plate capacitor shows a high capacitance tuning ratio, it fails to provide an equally high frequency tuning range.

Experimental results for the 2.4 GHz VCO (Fig. 4.5), employing the two-parallel-plate MEMS capacitor made up of polysilicon/gold have been presented in [15]. Table 4.3 provides a comparison between theoretical calculations, simulation results as obtained from COSMO and experimentally observed data based on the same initial design.

TABLE 4.2. COMPARISON OF DIFFERENT MEMS CAPACITOR STRUCTURES.

	Capacitance Tuning Ratio	Frequency Tuning Range
Cantilever Beam	1.18:1	6.4%
Fixed-Fixed Beam	1.27:1	0.6%
Polysilicon/Gold	1.43:1	14.6%
Aluminum	1.37:1	19.2%
Nickel/Gold	1.32:1	7.3%
Three-plate	1.88:1	23.28%

TABLE 4.3. COMPARISON OF SIMULATED RESULTS WITH THEORETICAL CALCULATIONS AND EXPERIMENTAL DATA.

	Theoretical Calculations	Simulated Results (this work)	Measured Results
Nominal Capacitance	0.6 pF	1.4 pF	1.4 pF
Capacitance tuning ratio	1.5:1	1.43:1	1.35:1
Pull-in Voltage	3.3 V	3.3 V	5.0 V
Frequency tuning range	18.35 %	14.6 %	3.4%

Although the MEMS capacitor was designed for a nominal capacitance of 0.6 pF, a capacitance of 1.4 pF was measured. This is due to the top plate and bottom plate parasitic capacitances and high pad parasitic capacitances. As described in the previous sections, these parasitic capacitances have been taken into account in the simulations. Measured results also show a lower tuning range at a higher pull-in voltage. This discrepancy in the tuning range with measured results can be attributed to residual stress which is a result of the fabrication process [12].

The VCO is simulated for a transient time of 60 μs. Each MEMS capacitor device makes 732 calls to EM8.9 during the transient run. EM8.9 takes approximately 3 mins to analyze 1089 discrete nodes for an applied voltage of 2.7 V. COSMO makes a total of 1464 device calls and requires approximately 73 hours of CPU time.

4.7. Dynamic Simulation Results

The dynamic behavior of MEMS variable capacitors is governed by the second order differential equation given by (3.10). Hence, like any other second-order system, the step response of the MEMS variable capacitor carries important information about its dynamic properties. The response of a fixed-fixed beam capacitor to a 1 V step input is shown in Fig. 4.13 for different values of the mechanical damping factor ζ (= $1/2Q_M$). It is seen that the fixed-fixed beam

capacitor exhibits a critically damped response for ζ=3 and the capacitance overshoots for ζ<3. Another important property of MEMS variable capacitors that comes into light is the settling time of the capacitance. For the fixed-fixed beam capacitor under consideration, the settling time is seen to be approximately 20 μs. Thus, the effect of this slow behavior of MEMS variable capacitors on the performance of RF VCOs can be inferred from the step response. As an example, for a 1 GHz MEMS VCO employing the fixed-fixed beam capacitor with a 1% capacitance settling time of 20 μs, it would take 20,000 cycles to attain its steady state frequency.

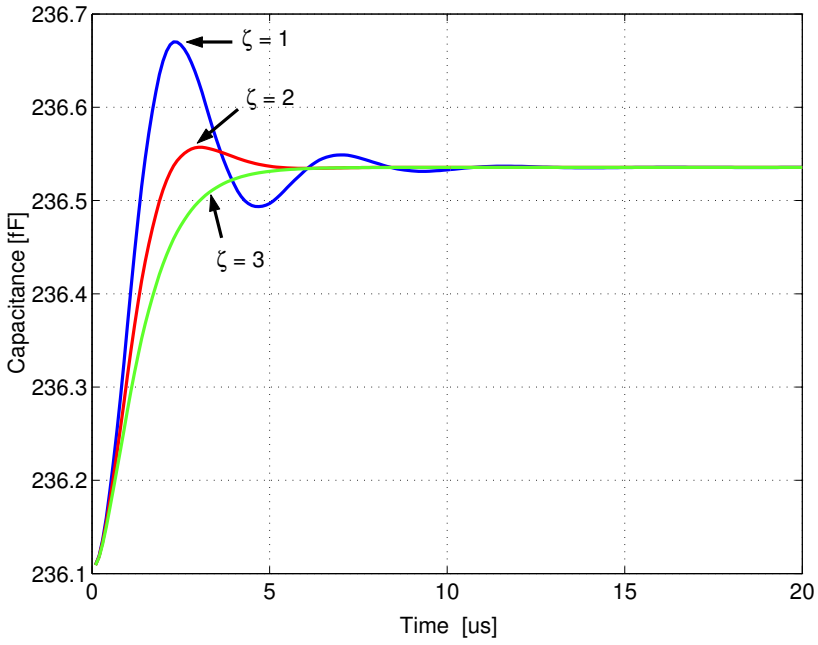

Fig. 4.13. Step response of a fixed-fixed beam capacitor.

The slow dynamic behavior of the MEMS variable capacitors also has an adverse impact on the simulation requirements of RF MEMS VCOs. Taking the example of the 1 GHz VCO and assuming that 100 time points per cycle are needed for an accurate transient simulation, 20,000 X 100 device calls need to be made. Since each call to the device takes 3 mins on the average, the total CPU time required would be approximately 4166 days! In addition to the extraordinarily large computational time, the high memory requirements make dynamic simulations of RF MEMS VCOs computationally expensive.

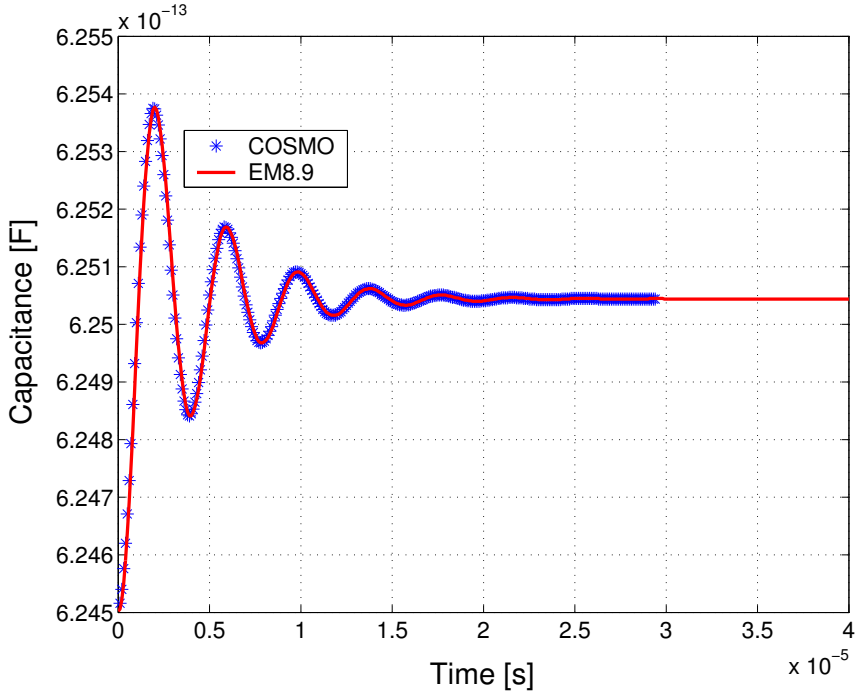

Fig. 4.14. Comparison of step response of MEMS capacitor obtained from EM8.9 and COSMO.

A time-stepping scheme as described in Section 4.4 is used in COSMO to improve its computational efficiency. However, the improvement provided by this scheme is insufficient for the dynamic simulation of MEMS VCOs operating at high frequencies. Therefore, in order to validate dynamic simulations in COSMO, the step response of a fixed-fixed beam capacitor obtained from a stand-alone EM8.9 run is compared with that obtained from COSMO. The results obtained from EM8.9 and COSMO are shown in Fig. 4.14 and are seen to be in good agreement. COSMO could be simulated only for a time interval of 29.8 μs while EM8.9 could be simulated for a maximum time of 39.8 μs before the system crashes due to a shortage of memory. COSMO requires approximately 3 hrs 30 min of CPU time and 2.14 GB of memory to simulate the step response shown in Fig. 4.14.

4.8. Summary and Missing Effects in COSMO

A coupled device and circuit simulator for the design of RF MEMS VCOs, COSMO, was described in this chapter. A method for the accurate computation of the capacitance of the MEMS variable capacitor was presented. The detailed coupling description in COSMO was discussed for static as well as dynamic simulations. A time-stepping scheme was presented to improve the computational efficiency for dynamic simulations. Simulated tuning characteristics of a 2.4 GHz RF MEMS VCO were illustrated for different MEMS capacitor structures and comparisons were made with experimentally observed data. Finally, the step

response of MEMS variable capacitors was discussed and dynamic simulation results were illustrated. The effects of the large capacitance settling time on RF MEMS VCO performance and on the simulation requirements in COSMO are also discussed. This chapter is concluded with a discussion on the missing effects in COSMO.

4.8.1. Residual Stress

In Section 4.6 it was mentioned that discrepancies in the simulated and measured tuning characteristics can be attributed to residual stress. During the fabrication process, the polysilicon layers are deposited at high temperatures. As these layers cool down to room temperature, a certain amount of residual stress develops due to the thermal expansion of polysilicon. Hence, the top capacitor plate tends to warp after the annealing and the sacrificial layer release. This alters the capacitance of the MEMS capacitor and therefore the frequency tuning characteristics of the VCO changes.

The residual stress can be modeled as a spring with spring constant k_r given by

$$k_r = 8\sigma(1-\nu)W\left(\frac{t}{L}\right) \tag{4.3}$$

where, σ is the biaxial residual stress, ν is the Poisson's ratio, W is the width, L is the length and t is the thickness of the top plate [12]. This equation holds true for a load distributed across the entire beam as is the case for electrostatically actuated MEMS variable capacitors. Thus the effect of residual stress on the tuning characteristics of MEMS capacitors can be analyzed by adding the equivalent spring constant k_r (4.3) to the spring constant of the suspension structures k_m (3.6). It should be noted that the addition of residual stress will further complicate the design of MEMS capacitors since k_r unlike k_s is a function of the dimensions of the top plate.

4.8.2. Effect of Holes in the Top Plate of MEMS Capacitors

In many MEMS varactors, small diameter holes are defined in the top plate to reduce the squeeze film damping [12]. The hole area can be up to 60% of the total surface area of the MEMS structure. The holes release some of the residual stress in the beam, and reduce the Young's modulus of the MEMS structure. The holes also result in a lower mass of the beam, which in turn yields a higher mechanical resonant frequency (3.11). Hence, the number and size of these holes in the top plate can be an important design consideration for MEMS variable capacitors and therefore should be accounted for in COSMO.

5 SIMULATION OF PHASE NOISE IN RF MEMS VCOS

5.1 Introduction

Oscillator phase noise is a key parameter for high-performance communication systems. In a conventional LC oscillator, the electrical thermal noise, and 1/*f* noise contribute to phase noise. However, in a micromachined-based LC-tuned oscillator, additional phase noise is generated due to the mechanical thermal vibrations of the tunable capacitors. In this chapter, phase noise resulting from both electrical noise sources and micromachined noise sources is mathematically analyzed. The theoretical analysis is based on an LTI system assumption. Based on this analysis, phase noise from both electrical and mechanical noise sources is compared and their combined effect on the overall phase noise of MEMS VCOs is discussed. Although the LTI system approach of analyzing phase noise is known to be inaccurate, it is sufficient for comparison purposes. For accurate estimation of phase noise a simulation environment is employed. The simulation method is based on a nonlinear circuit-level noise analysis where the time-variant property of oscillators is taken into account. The VCO circuit used for phase noise simulations is described and simulation results are illustrated. The simulated phase noise characteristics are compared with theoretical deductions. Finally, a comparison with experimental data is provided

and some important issues regarding phase noise in RF MEMS VCOs are addressed.

5.2 Phase Noise in RF MEMS VCOs

A MEMS-based parallel LC-tuned oscillator can be represented as shown in Fig. 5.1. It consists of an ideal G_m stage, a tank circuit and a positive feedback loop. The tank circuit consists of an ideal inductor L, the parallel equivalent of the series resistance of the inductor R_P, the MEMS variable capacitor C_D, and the total tank parasitic capacitance C_P. The resistor and the MEMS capacitor constitute the

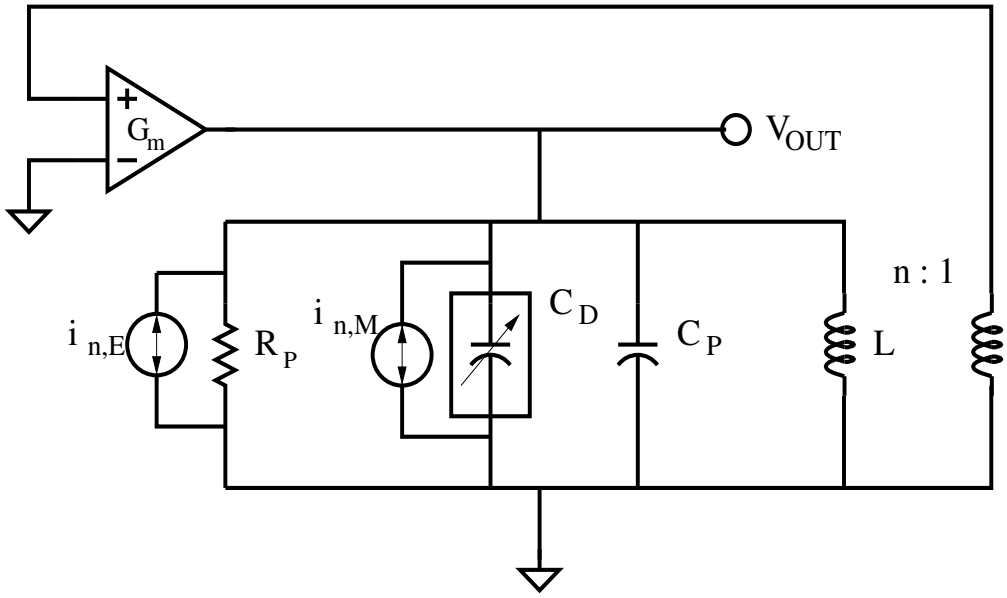

Fig. 5.1. MEMS-based parallel LC-tuned oscillator.

noisy elements in the tank and their equivalent current noise sources are denoted by $i_{n,E}$ and $i_{n,M}$ respectively. Both the electrical input noise ($i_{n,E}$) and the mechanical input noise ($i_{n,M}$) result in phase noise at the output of the oscillator.

5.2.1 Phase Noise from Electrical Noise Sources

In conventional LC-tuned oscillators, the dominant contributor of phase noise is the electrical thermal noise. Thermal noise in the resistor R is represented by a parallel current noise source with power spectral density given by

$$\frac{\overline{i_n^2}}{\Delta f} = \frac{4k_B T}{R} \tag{5.1}$$

where, k_B is the Boltzmann's constant and T is the absolute temperature. Phase noise due to thermal noise can be determined by employing a transfer function approach based on a linear time-invariant (LTI) system. The transfer function from the noise current source $i_{n,E}$ to the output can be approximated by [14]

$$T_{n,E}^2(\omega_0 + \Delta\omega) = \frac{1}{4(\omega_0 C)^2}\left(\frac{\omega_0}{\Delta\omega}\right)^2 \tag{5.2}$$

where, $C = C_D + C_P$ is the total tank capacitance, ω_0 is the carrier frequency, and $\Delta\omega$ is the frequency offset from the carrier. Using the above equations, the oscillator phase noise due to electrical thermal noise can be calculated as

$$S_\theta(\Delta\omega)_E = \frac{\overline{v_{noise}^2}}{\overline{v_{signal}^2}} = \frac{\frac{1}{2}\cdot T_{n,E}^2(\omega_0 + \Delta\omega)\cdot \overline{i_{n,E}^2}}{\frac{1}{2}V_{amplitude}^2} \tag{5.3}$$

where, the factor of ½ in the noise power arises from separating the amplitude modulation component from the phase modulation component [13]. Substituting (5.1) and (5.2) in (5.3), and simplifying we obtain the final expression for the oscillator phase noise due to thermal noise given by

$$S_\theta(\Delta\omega)_E = \frac{kT}{2P_{rf}Q^2}\left(\frac{\omega_0}{\Delta\omega}\right)^2 \tag{5.4}$$

where, P_{rf} is the oscillator RF output power and Q is the quality factor of the tank circuit. The above expression does not include the contribution of device 1/*f* noise. In practice, 1/*f* noise from the electronic devices gets up-converted and appears as a skirt around the carrier frequency, with a slope of 30 dB per decade. For offset frequencies higher than the 1/*f* corner frequency, the phase noise is entirely due to white thermal noise and decays with a slope of 20 dB per decade.

5.2.2 Brownian-Motion-Induced Phase Noise

In addition to the classical phase noise described above, a MEMS-based LC-tuned oscillator introduces additional phase noise due to the mechanical-thermal vibration, also known as Brownian motion, from the variable capacitors. The displacement noise power spectral density can be computed as [17], where b is the damping coefficient due to surrounding gas ambient and the internal dissipation of the system, k_m is the spring constant, ω_n is the mechanical resonant frequency, and Q_M is the mechanical quality factor.

$$\frac{\overline{X_n^2(\omega)}}{\Delta f} = \frac{4k_B T b}{k_m^2\left[\left(1-\frac{\omega^2}{\omega_n^2}\right)^2 + \frac{1}{Q_M^2}\frac{\omega^2}{\omega_n^2}\right]} \tag{5.5}$$

This expression for the displacement noise power spectral density can be readily arrived at by multiplying the input force to displacement transfer function, *H(s)*, (3.11) with the equivalent noise force given by [17]

$$F_N = \sqrt{4k_B T b} \tag{5.6}$$

For frequencies below and above ω_n, (5.5) evaluates the displacement noise power spectral density to be $4k_BT/mQ_M\omega_n^{\,3}$ and $4k_BT\omega_n/mQ_M\omega^{\,4}$, respectively. At

resonance the noise power spectral density can be computed to be $4k_BTQ_M/m\omega_n{}^3$. Fig. 5.3 illustrates the displacement noise PSD for different values of Q_M for a typical MEMS capacitor design. The noise spectrum is white for frequencies below ω_n and falls with a slope of 40 dB per decade for frequencies higher than ω_n. It can also be seen that the displacement noise decreases with an increase in Q_M for frequencies below and above ω_n. However, peaks are seen at the mechanical resonant frequency for Q_M greater than $1/\sqrt{2}$. In addition, the magnitude of these peaks increase with an increase in the value of Q_M.

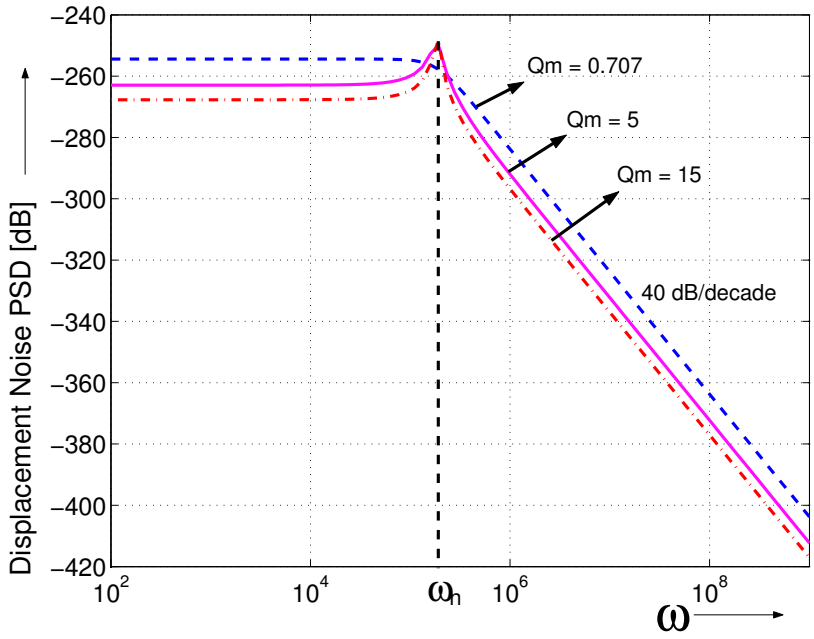

Fig. 5.2. Displacement noise power spectral density.

The noisy vibrations of the suspended plate cause variations in the capacitance value and hence output phase noise. The equivalent input current noise power spectral density can be computed by observing the current that arises from the change in capacitance due to Brownian motion. When a signal, v_{sig}, is applied across the MEMS capacitor, the displacement of the top plate is modulated around the DC bias displacement x_{dc} corresponding to an applied voltage $v_{sig(rms)}$ [12]. The current noise that arises due to the change in the steady state capacitance can be expressed as a function of the displacement noise due to Brownian motion as given by (5.7).

$$i_{n,M} = v_{sig\,(rms)} \cdot \frac{\partial C_D}{\partial t} = v_{sig\,(rms)} \cdot \left(\frac{\partial C_D}{\partial x}\right) \cdot \left(\frac{\partial x}{\partial t}\right)_{noise} \tag{5.7}$$

For a signal frequency corresponding to the oscillation frequency ω_0, (5.7) can be simplified to obtain the current noise power spectral density expressed as

$$\overline{i_{n,M}^2} = \frac{\omega_0^2 C_D^2 V_{amplitude}^2}{2(d+x)^2} \overline{X_n^2(\omega)} \tag{5.8}$$

where, $V_{amplitude}$ is the amplitude of oscillation and $\overline{X_n^2(\omega)}$ is the displacement noise power spectral density. In order to determine a theoretical expression for the phase noise due to Brownian motion, we again use the transfer function approach. From

Fig. 5.1 it is evident that the transfer function from the noise current source $i_{n,,M}$ to the output is the same as given by (5.2) and can be expressed as

$$T_{n,M}^2(\omega_0 + \Delta\omega) = \frac{1}{4\omega_0^2 C_D^2 (1+\eta)^2}\left(\frac{\omega_0}{\Delta\omega}\right)^2 \tag{5.9}$$

where, $\eta = C_P/C_D$ is the ratio of the tank parasitic capacitance to the desired capacitance. Using (5.8) and (5.9) in (5.3), we obtain the oscillator phase noise due to Brownian motion or mechanical-thermal vibration given by (5.10).

$$S_\theta(\Delta\omega)_M = \frac{\overline{X_n^2(\omega)}}{8(1+\eta)^2(d+x)^2}\left(\frac{\omega_0}{\Delta\omega}\right)^2 \tag{5.10}$$

From (5.5) and (5.10), phase noise due to the Brownian motion is seen to decrease at 20 dB and 60 dB per decade below and above the offset frequency, ω_n, respectively. At ω_n offset frequency the phase noise is enhanced due to peaking in the capacitor displacement noise power spectral density (Fig. 5.2).

From (5.4) and (5.10), the phase noise profiles due to Brownian-motion, $S_\theta(\Delta\omega)_M$, and electrical thermal noise, $S_\theta(\Delta\omega)_E$, are plotted in Fig. 5.3 for a typical design condition. It is apparent that the Brownian-motion-induced phase noise is dominant for low offset frequencies. However, it decreases much faster than the classical phase noise above the mechanical resonant frequency, ω_n, and eventually

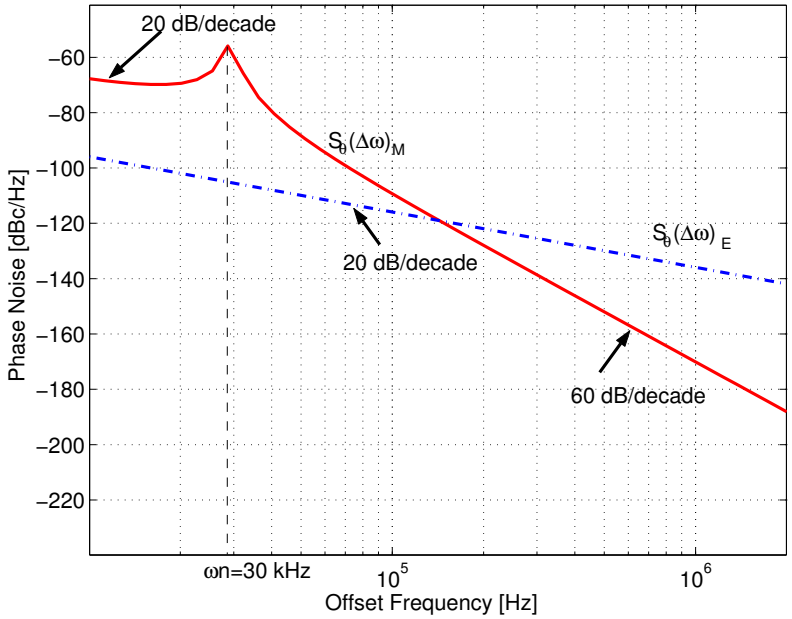

Fig. 5.3. Theoretical phase noise profiles of a MEMS VCO.

phase noise due to electrical thermal noise dominates. Peaking is observed in the phase noise profile at the mechanical resonant frequency. These peaks will increase as Q_M increases. Device 1/*f* noise has not been taken into account here. In practice, 1/*f* noise results in an increased noise level for low offset frequencies.

The phase noise analysis discussed so far is based on an LTI system assumption for oscillators. The simplicity associated with the analysis of LTI systems is taken advantage of to gain an intuitive insight of the phase noise characteristics of RF MEMS

VCOs. Furthermore, the contribution of electrical noise sources as well as mechanical noise sources to the overall phase noise performance of RF MEMS VCOs is studied and compared. However, phase noise analysis based on such an LTI system is known to be inaccurate since oscillators are fundamentally time-varying systems [14]. Thus, although the analysis described above is sufficient to study the trends of phase noise in MEMS VCOs, it may lead to sub-optimal results. Hence, an analysis based on a LTV system must be employed for the accurate simulation of phase noise.

5.3 Phase Noise Simulations

The coupled simulator COSMO handles phase noise analysis based on a non-linear perturbation analysis for oscillators [18–21]. The implemented technique allows for an accurate simulation of phase noise due to devices described either by analytical or numerical models.

For $0 \leq \Delta\omega << \omega_0$, the single-sideband phase noise spectrum $L(\Delta\omega)$ in *dBc/Hz* can be approximated as [21]:

$$L(\Delta\omega) = 10\log_{10}\left(\frac{4\omega_0^2 c(\Delta\omega)}{\omega_0^4 c^2(\Delta\omega) + 4\Delta\omega^2}\right) \tag{5.11}$$

where, the scalar constant $c(\Delta\omega)$ is frequency dependent. In the general case, $c(\omega)$ is given by:

$$c(\omega) = c_w + \sum_{m=1}^{M} |c_{cm}(\omega)|^2 \tag{5.12}$$

where c_w is a contribution to the scalar c from white noise sources and is given by:

$$c_w = \frac{1}{T}\int_0^T v_1^T(\tau) B_w(x_s(\tau)) B_w^T(x_s(\tau)) v_1(\tau) d\tau \tag{5.13}$$

and c_{cm} is the contribution to the scalar c from the m-th colored noise source and is given by:

$$c_{cm} = \frac{1}{T}\int_0^T v_1^T(\tau) B_{cm}(x_s(\tau)) d\tau \tag{5.14}$$

where $v_1(\tau)$ is the perturbation projection vector (PPV) [21] and B_w and B_{cm} are described later. The PPV is a periodic vector which serves as a transfer function from the noise sources to the scalar c, and hence to the overall phase noise power spectral density. The PPV scales the amount of noise transferred to the scalar c at

each point of time. B_w is a state-dependent matrix that maps white noise sources with unity PSD to the system of differential algebraic equations (DAEs) which describe a circuit. B_{cm} is a state-dependent vector that maps the m-th colored noise source to the system of DAEs. Thus, in order to obtain the single-sideband phase noise spectrum $L(\Delta\omega)$ in dBc/Hz, first a scalar c (5.12) needs to be calculated using (5.13) and (5.14) followed by computation of the phase noise spectrum using (5.11). The method to obtain the PPV and matrices B_w and B_{cm} is described in [18].

The first part of the algorithm is implemented in the transient analysis routine, where all the necessary data is collected and saved. The second part of the algorithm, which deals with the phase noise calculation itself, is implemented as a separate analysis (pnoise analysis). The sequence of operations is as follows. First, a transient analysis is run for a long enough time to ensure that the circuit reaches a steady state. During transient analysis, the period of oscillation T is calculated and necessary data is saved from a time interval of one period for phase noise calculation. At each time point of this time interval, the C (capacitance) and G (conductance) circuit matrices are saved, state-dependent noise sources are evaluated and the matrix B_w (for white noise sources) and the vectors B_{cm} (for colored noise sources) are stamped and saved.

In order to compute the additional phase noise due to the MEMS capacitor, the equivalent input noise needs to be evaluated. The equivalent input current noise PSD can be easily computed using (5.5) and (5.8). The capacitance C_D and the displacement x are obtained from the device simulator EM8.9 while the frequency

of oscillation ω_0 and the amplitude of oscillation $V_{amplitude}$ are obtained from a transient analysis.

The phase noise calculation routine starts with the perturbation projection vector calculation (PPV) and then the scalar c is calculated. Finally, the single-sideband phase noise spectrum $L(\Delta\omega)$ in dBc/Hz is calculated using (5.11).

5.4 MEMS VCO Design for Phase Noise Simulations

In order to validate the phase noise simulations performed by COSMO, an existing VCO circuit is used as the test circuit. Simulation results obtained from COSMO are verified with existing experimental data. Appropriate comparisons and illustrations of results are presented in the next section. In this section the VCO test circuit is presented and design considerations for the MEMS variable capacitor are described.

5.3.1 The VCO Circuit

An 800 MHz single-ended Colpitts VCO [13] implemented in a HP 0.8 µm CMOS technology was simulated to validate the phase noise simulations. The schematic of the VCO is as shown in Fig. 5.4. The oscillator consists of a common gate amplifier with a small-signal transconductance of 30 mA/V. Two capacitors (C_1 = 1 pF and C_2 = 4 pF) are used to form a feedback path with a feedback ratio of

5:1. An ideal 8.2 nH inductor with a quality factor, Q_L, of 30 is used as a part of the tunable resonator. This inductance value is chosen to resonate with an overall tank capacitance, C_{Tank}, at 800 MHz. C_{Tank} can be expressed as

$$C_{Tank} = C_{MEMS} + \frac{C_1 C_2}{C_1 + C_2} + C_P \tag{5.15}$$

where, C_{MEMS} is the MEMS variable capacitance and C_P represents the tank parasitic capacitance which is taken to be 2 pF in this design. In order to ensure reliable oscillation start up, the small-signal loop gain must be at least equal to 4 [14]. Thus, the condition for start up of oscillations is given as

$$\frac{g_m R}{n}\left(1 - \frac{1}{n}\right) \geq 4 \tag{5.16}$$

where, g_m is the small-signal transconductance of the amplifier, $1/n = C_1/(C_1+C_2)$ is the capacitive voltage divider ratio, and R is the tank impedance. Hence, with g_m=30 mA/V and n=5, the tank impedance, R, required for start up is calculated to be 850 Ω which corresponds to an overall tank quality factor of approximately 20 at 800 MHz.

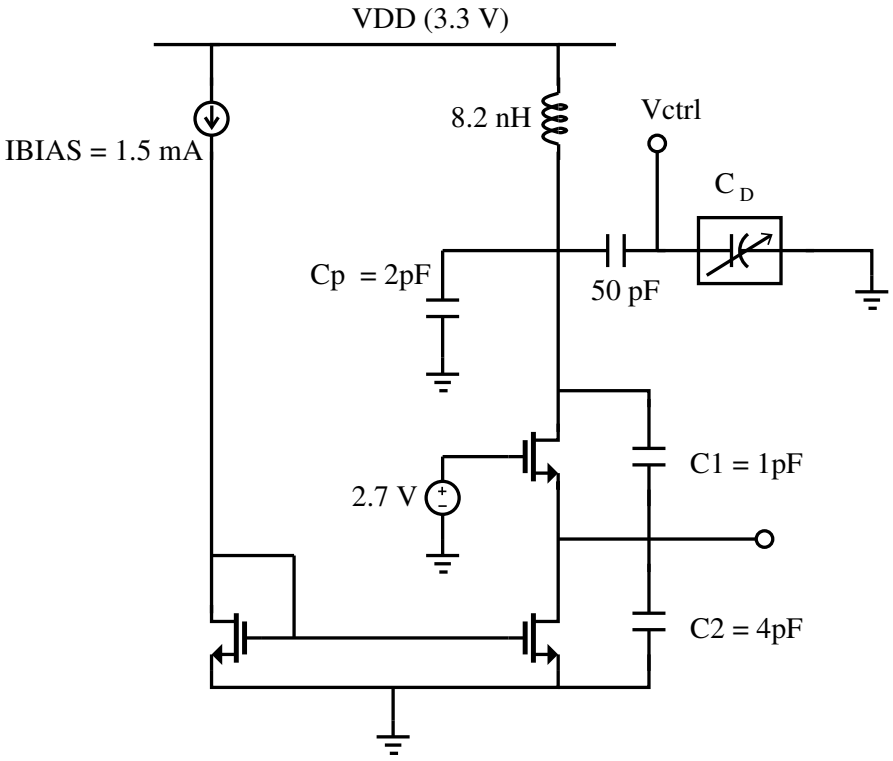

Fig. 5.4. VCO circuit for phase noise simulations.

In a typical VCO, the overall tank quality factor, $Q_{Tank,}$ can be expressed as the parallel equivalent of the inductance quality factor, Q_L, and the quality factor of the variable capacitor, Q_C and can be expressed as

$$Q_{Tank} = Q_L \parallel Q_C = \frac{Q_L Q_C}{Q_L + Q_C} \tag{5.17}$$

From (5.17) and with Q_L taken as 30, Q_C must be equal to 60 in order to achieve a Q_{Tank} of 20 to ensure start up of oscillations.

5.3.2. MEMS Variable Capacitor Design

A two-parallel-plate MEMS variable capacitor (Fig. 3.3) was designed for an overlap area of 200 µm x 200 µm and an air-gap of 1.5 µm to obtain a nominal capacitance of 0.2 pF. However, due to the top plate parasitic capacitance, a nominal capacitance of 0.5 pF is obtained. Four of these capacitors are connected in parallel for a total nominal capacitance of 2 pF. For a tuning voltage of 3 V, a maximum capacitance tuning ratio of 1.5:1 can be achieved by a suspension spring constant of 3.8 N/m (3.3). The mass of the suspended top plate is taken as 100 ng corresponding to a mechanical resonant frequency of 30 kHz. The suspension structures are designed to achieve the desired stiffness constant of k_m = 3.8 N/m and the required quality factor, Q_C = 60.

5.5 Simulation Results and Validation with Experimental Data

The MEMS VCO described in the previous section was simulated using COSMO. The capacitance of the MEMS capacitor as a function of the tuning voltage is as shown in Fig. 5.5. For a tuning voltage of 3 V, the capacitance varies from 236 fF to 325.5 fF, providing a maximum capacitance tuning ratio of 1.38:1.

A stiffness constant of k_m = 3.4 N/m for the suspension structures is used in the simulations to achieve the maximum capacitance tuning ratio. Based on the initial design described in the previous section, Table 5.1 provides a comparison between simulation results and measurement results.

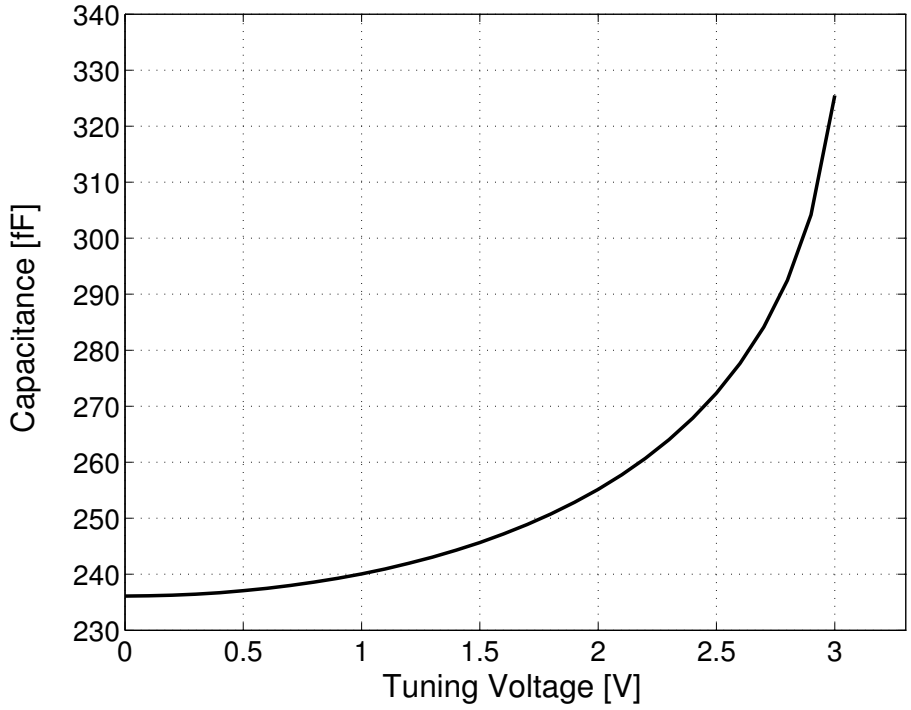

Fig. 5.5. Capacitance as a function of voltage for the MEMS capacitor.

TABLE I. COMPARISON BETWEEN SIMULATION AND MEASUREMENT RESULTS BASED ON THE SAME INITIAL DESIGN (ω_n = 30 kHz, ω_0 = 800 MHz).

	Simulation	**Measurements** [13]
Cap. tuning ratio	1.38 : 1	1.16 : 1
Tuning voltage	3 V	5.5 V
Mech. resonant freq. (ω_n)	29.3 kHz	20 kHz
Oscillation freq. (ω_o)	787 MHz	721 MHz

From (5.5) and (5.8) it can be seen that the phase noise due to noise in the MEMS capacitor is a function of the oscillation frequency ω_0 and the mechanical resonant frequency ω_n. Therefore, in order to ensure valid comparisons between simulated phase noise and that obtained from measurements, it is important that ω_0 and ω_n be the same for both cases. Hence, the tank parasitic capacitance C_P is increased to 3 pF in order to obtain a simulated oscillation frequency of 721 MHz and a higher value for the mass of the top plate of the MEMS capacitor (215.3 ng) is chosen to obtain a simulated mechanical resonant frequency of 20 kHz.

The simulated phase noise spectrum of the modified MEMS VCO is shown in Fig. 5.6. The contribution of the individual noise sources is also illustrated. The simulated phase noise characteristics are in good agreement with the theoretical phase noise profile discussed in Section 5.2 (Fig. 5.3). At low offset frequencies, device 1/*f* noise dominates and, therefore, the phase noise of the MEMS VCO shows a 30 dB per decade fall. For frequencies higher than the mechanical resonant frequency of 20 kHz, the electrical-thermal noise dominates and the phase noise

shows a decay of 20 dB per decade. At an offset frequency equal to the mechanical resonant frequency ω_n=20kHz, the phase noise is enhanced due to the peaking in the mechanical-thermal noise power spectral density at mechanical resonance.

Analysis of (5.5) and (5.8) shows that the only way to suppress the additional phase noise contributed by the MEMS capacitor, without altering its design parameters, is by increasing Q_M . However, it is also seen that at the mechanical resonance frequency the phase noise is enhanced due to the increased

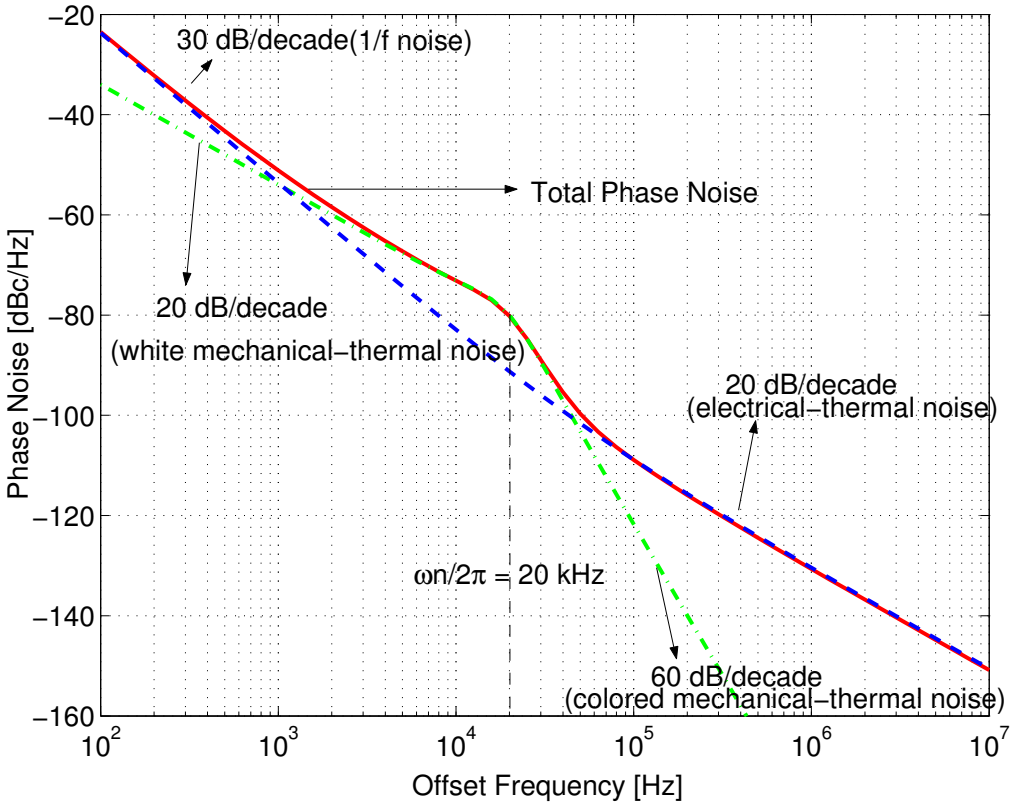

Fig. 5.6. Simulated phase noise spectrum (Q_M = 1) of the MEMS VCO and contribution of the different noise sources.

Q_M. The measured output power spectrum of the VCO under consideration reveals two main side-band peaks occurring at 20 kHz away from the carrier [13]. The simulated phase noise spectrum for different values of Q_M has been shown in Fig. 5.7. It can be seen that the peaks occur at the mechanical resonance frequency, i.e., at 20 kHz offset from the carrier. It can also be observed that the magnitude of the peaks increase with an increase in Q_M.

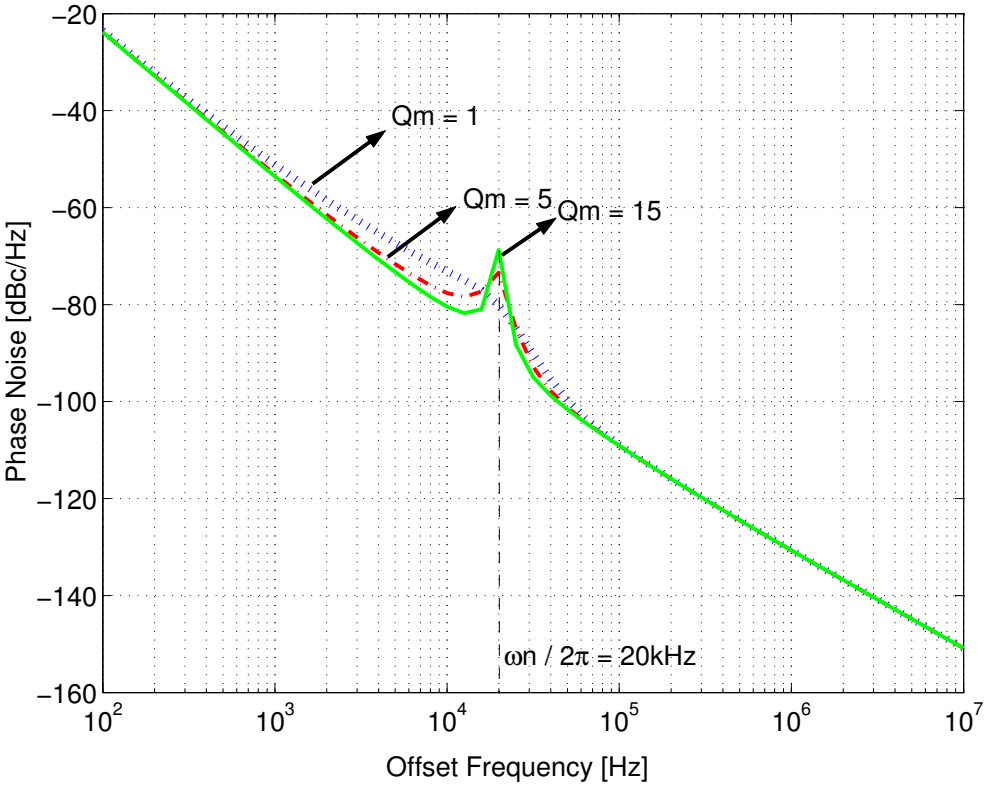

Fig. 5.7. Simulated phase noise spectrum (Q_M = 1, 5, 15) of MEMS VCO.

Table 5.2 provides the simulated values of the total phase noise for different values of Q_M. An improvement in the phase noise can be seen for increasing Q_M for low offset frequencies. However, as the offset frequency gets higher, the dependence of phase-noise on Q_M reduces. The table also provides a comparison between simulated and measured data for phase noise. It can be seen that they are in good agreement.

TABLE 5.2. SUMMARY OF PHASE NOISE SIMULATIONS AND COMPARISON WITH MEASURED DATA.

Offset Frequencies	**Measured (Q_M = 15)**	**Simulated (Q_M = 15)**	**Simulated (Q_M = 5)**	**Simulated (Q_M = 1)**
10 kHz	-81	-80.4	-77.6	-73.1
100 kHz	-110	-109.1	-109.1	-108.9
3 MHz	-139	-140.8	-140.8	-140.8

5.6 Summary

Phase noise in RF MEMS VCOs is discussed in detail in this chapter. A simplified mathematical analysis of phase noise in MEMS VCOs is presented and important observations are addressed based on a theoretical phase noise analysis. An accurate expression for the equivalent input current noise PSD is presented. This expression for the current noise PSD is used to derive an approximate expression for the additional phase noise due to MEMS variable capacitors. In addition, a simulation method used in COSMO to accurately simulate the phase noise of RF MEMS VCOs is described. Simulation results of a single-ended Colpitts VCO are illustrated and comparisons are made with measured data. It is seen that MEMS variable capacitors do not affect the phase noise at offset frequencies sufficiently far away (lower and higher) from the mechanical resonant frequency. However, phase noise near the mechanical resonant frequency is enhanced due to an increase in the mechanical quality factor of the MEMS capacitor. This results in peaks in the output power spectrum of the VCO. It has been shown that the simulated results follow similar trends with theory and are in good agreement with experimental data.

6 CONCLUSIONS

6.1 Summary

A novel coupled circuit and device simulator, COSMO, is developed for the design of low-phase noise RF MEMS VCOs. The simulator successfully simulated a wide variety of MEMS capacitor structures, ranging from the simplest cantilever and fixed-fixed beam capacitors to the novel and recent three-parallel-plate, wide tuning range MEMS capacitor. The effect of different structural materials for the MEMS-based capacitors on the overall performance of the VCO was presented. A simulation method to accurately simulate the phase noise of RF MEMS VCOs was also described. Simulated results were compared with experimentally observed behavior. The observed discrepancies can be attributed to combined effects of parasitic capacitances and residual stress. The simulator provides accurate results and can be used for the improved design of RF MEMS VCOs.

6.2 Future Work

The goal of this research project is to develop an accurate as well as computationally efficient simulator for design of RF MEMS VCOs. This work focuses on the accuracy aspect of the coupled simulator, COSMO. COSMO is

capable of simulating the two important performance parameters of RF MEMS VCOs, tuning characteristics and phase noise. Comparisons with experimentally observed behavior showed that the simulated phase noise is in good agreement with measured data. However, discrepancies were observed between the tuning characteristics obtained from simulations and that obtained from experiments. The effects that cause these discrepancies have been discussed and can be easily incorporated in COSMO.

Future work should focus on improving the computational efficiency of COSMO. The CPU time and memory requirements for static simulations can be decreased by a prudent restructuring of the device simulator, EM8.9. Accurate dynamic simulations are important to study the behavior of RF MEMS VCOs operating within a phase-locked loop (PLL) environment. A more efficient time-stepping algorithm can be developed for dynamic simulations in COSMO by employing an implicit integration method for transient analysis in EM8.9. It was discussed how the slow dynamic behavior of MEMS variable capacitors makes it difficult to study their steady-state behavior by using transient analysis. Hence, a periodic steady state (PSS) analysis can be employed in COSMO to obtain the steady-state solution. Furthermore, the phase noise calculation technique can be implemented in combination with the PSS analysis to improve the accuracy and reduce the time for phase noise simulations in COSMO.

BIBLIOGRAPHY

[1] W. L. Engl, R. Laur, and H. K. Dirks, "MEDUSA – a simulator for modular circuits," *IEEE Trans. Computer-Aided Design*, vol. 1, pp. 85-93, Apr. 1982.

[2] K. Mayaram, "CODECS: A mixed-level circuit and device simulator," *Memo No. UCB/ERL M88/77*, Electronics Research Laboratory, University of California, Berkeley, Nov. 1988.

[3] T. L. Quarles, "The SPICE3 implementation guide," *Memo No. UCB/ERL M89/44*, Electronics Research Laboratory, University of California, Berkeley, Nov. 1989.

[4] K. Mayaram, P. Yang, and J. Chern, "Transient three-dimensional mixed-level circuit and device simulation: algorithms and applications," *IEEE Int. Conf. on Computer-Aided Design*, pp. 112-115, Nov. 1991.

[5] K. Mayaram and D. O. Pederson, "Coupling algorithms for mixed-level circuit and device simulation," *IEEE Trans. Computer-Aided Design*, vol. 11, pp. 1003-1012, Aug. 1992.

[6] R. M. Kirby, G. E. Karniadakis, O. Mikulchenko, and K. Mayaram, "An integrated simulator for coupled domain problems in MEMS," *IEEE/ASME Journal of Microelectromechanical Systems*, vol. 10, pp. 379-391, Sept. 2001.

[7] T. Dudar, "Algorithms and simulators for coupled device/circuit simulation," *M. S. Thesis*, Oregon State University, December 2002.

[8] W. J. McCalla and D. O. Pederson, "Elements of computer-aided circuit analysis," *IEEE Trans. Circuit Theory*, vol. ct-18, pp. 14-26, Jan. 1971.

[9] S. D. Senturia, N. Aluru, and J. White, "Simulating the behavior of MEMS devices: computational methods and needs," *IEEE Computational Science and Engineering*, pp. 30-43, Jan. 1997.

[10] G. Li and N. R. Aluru, "Efficient mixed-domain analysis of electrostatic MEMS," *IEEE Transactions on Computer-Aided Design of Integrated Circuits and Systems*, Vol. 22, No. 9, pp. 1228-1242, 2003.

[11] A. Dec and K. Suyama, "Micromachined electromechanically tunable capacitors and their applications to RF ICs," *IEEE Trans. Microwave Theory Tech.*, vol. 46, pp. 2587-2595, Dec. 1998.

[12] G. M. Rebeiz, *RF MEMS Theory, Design, and Technology*, John Wiley & Sons, 2003.

[13] D. J. Young, "Micromechanical Devices and Fabrication Technologies for Radio-Frequency Analog Signal Processing," *Memo No. UCB/ERL M99/24*, Electronics Research Laboratory, Univ. of California, Berkeley, 1999.

[14] T. H. Lee, *The Design of CMOS Radio-Frequency Integrated Circuits,* Cambridge University Press, Jan. 1998.

[15] A. Dec and K. Suyama, "Microwave MEMS-based voltage-controlled oscillators," *IEEE Trans. Microwave Theory Tech.*, vol. 48, pp.1943-1949, Nov. 2000.

[16] J. Sankaranarayan, M. Behera, N. Aluru, and K. Mayaram, "Accuracy issues in a high-level model for MEMS varactors," *IEEE BMAS Conf.*, pp.144-148, Oct. 2003.

[17] T. B. Gabrielson, "Mechanical-thermal noise in micromachined acoustic and vibration sensors," *IEEE Trans. Electron Devices*, vol. 40, pp. 903-909, May 1993.

[18] V. Kratyuk, "Algorithms and tools for optimization of integrated RF VCOs," *M.S. Thesis*, Oregon State University, June 2003.

[19] A. Demir, A. Mehrotra, and J. Roychowdhury, "Phase noise in oscillators: a unifying theory and numerical methods for characterization," *IEEE Trans. Circuit Syst.-I*, vol. 47, pp. 655-674, May 2000.

[20] A. Demir, "Phase noise in oscillators: DAEs and colored noise sources," in *Proc. IEEE/ACM Int. Conf. CAD*, pp. 170-177, Nov. 1998.

[21] A. Demir, "Floquent theory and non-linear perturbation analysis for oscillators with differential-algebraic equations," *International Journal of Circuit Theory and Applications*, pp. 163-185, Mar-Apr. 2000.

APPENDICES

APPENDIX A MEMS Capacitor Model Parameters

This appendix contains descriptions of the MEMS capacitor model parameters used by COSMO. The default values of these model parameters are also provided.

MODEL PARAMETER	DESCRIPTION	DEFAULT VALUE
captype	1 : cantilever beam capacitor 2 : fixed-fixed beam capacitor 3 : two-parallel-plate capacitor 4 : three-parallel-plate capacitor	1
simtype	1 : static simulations 2 : dynamic simulations	1
pullin	Pull-in voltage of the MEMS capacitor determined *a-priori*.	10 volts
maxiter	Maximum number of EM8.9 iterations allowed. If the number of EM8.9 iterations exceeds this value, it implies that the applied voltage has exceeded the pull-in voltage.	20
tpthick	Thickness of the top plate or the suspended plate.	1.5 µm
bpthick	Thickness of the bottom plate or the fixed plate.	2 µm 3

TpBpratio	Ratio of length of bottom (fixed) plate to length of top (suspended) plate. (always greater than 1)	1.5
tpxelem	Number of discrete elements along the length (x-axis) of the top (suspended) plate.	201
tpyelem	Number of discrete elements along the thickness (y-axis) of the top (suspended) plate.	9
bpxelem	Number of discrete elements along the length (x-axis) of the bottom (fixed) plate.	301
bpyelem	Number of discrete elements along the thickness (y-axis) of the bottom (fixed) plate.	9
ym	Young's modulus of elasticity of the material.	1.69e+7 Pa
km	Stiffness constant of the suspension structures. This parameter needs to be specified only for two-parallel-plate (captype = 3) and three-parallel-plate (captype = 4) structures.	44 N/m
mass	Mass of the top (suspended) plate. This parameter needs to be specified only for dynamic simulations (simtype=2).	1e-10 kg
qm	Mechanical quality factor. This parameter needs to be specified only for dynamic simulations (simtype = 2).	1

APPENDIX B Input Syntax for the MEMS Capacitor Device

The MEMS capacitor structure employed in this work can be broadly divided into two terminal and three terminal devices. The cantilever beam capacitor, fixed-fixed beam capacitor and the two-parallel-plate capacitor are modeled as two terminal devices. The three-parallel-plate capacitor is modeled as a three terminal device. The general form of the input line for the MEMS capacitor device is as shown below:

N1 node1 node2 {node3} Nx w=230u l=230u dg=0.75u {pg=0.75u}

.model Nx N captype=3 simtype=1 pullin=3.3

where, *N1* = name of device,

node1 = positive terminal of device (fixed plate),

node2 = negative terminal of device (suspended plate),

node3 = second positive terminal for three terminal device,

Nx = MEMS capacitor model name,

w = width of suspended plate,

l = length of suspended plate,

dg = nominal gap between suspended plate and fixed plate,

pg = nominal gap between the suspended plate and the second fixed plate for the three terminal device.

The parameters within braces denote that they are applicable only for three terminal devices. Hence, depending on the type of capacitor being employed, the device can exhibit a two-terminal or a three-terminal behavior.